Economic Geology, v. 105, pp. 1005–1023

Microbial Sphalerite Formation in Carbonate-Hosted Zn-Pb Ores, Bleiberg, Austria: Micro- to Nanotextural and Sulfur Isotope Evidence

H. Kucha,[1] E. Schroll,[2,°] J. G. Raith,[3,†] S. Halas[4]

[1]*University of Mining and Metallurgy, Faculty of Geology, Geophysics, and Environmental Protection, PL-30-059 Krakow, Poland*

[2]*University of Vienna, Institute of Mineralogy and Crystallography, Faculty of Geosciences and Geography, A-1090 Wien, Austria*

[3]*University of Leoben, Department of Applied Geosciences and Geophysics, A-8700 Leoben, Austria*

[4]*M. Curie-Sklodowska University, Institute of Physics, 20-031 Lublin, Poland*

Abstract

Microglobular sphalerite (90–180 μm) is a major form of sphalerite in the abandoned, Triassic carbonate-hosted Zn-Pb deposit at Bleiberg, Austria. It is common in ores from the Crest horizon and the first Cardita horizon, which contain about 0.5- to 3-mm-thick and up to 5-cm-long, wavy, discontinuous, sphalerite-rich bands composed of agglomerations of microglobular sphalerite. Based on comparisons with modern environments, these textures are interpreted as peloids and probably represent fossil microbial mats. These are interlayered with carbonate- and marcasite-rich, as well as finely banded, sphalerite layers (±fibrous galena and relics of oxysulfides), resulting in the characteristic rhythmically banded macrotexture of these Zn-dominated ores.

Microbial nanotextures, made visible by field emission scanning electron microscopy (FESEM) after etching, include sphalerite nanospheres (10–90 nm) and bacterial filaments. The sphalerite nanospheres are identical to those previously reported for mixed calcite-sphalerite peloids from Bleiberg and are very similar to nanotextures observed in recent bacterial biofilms made by Desulfobacteriaceae. The observed sphalerite nanospheres are interpreted as in situ metabolic products of sulfate-reducing bacteria. Micro- and nanotextures suggest that the larger, μm-sized sphalerite globules formed by agglomeration of sphalerite nanospheres, as well as by replacement of peloids representing former bacterial colonies; the latter are now composed of Zn-calcite cores surounded by serrated sphalerite rims. Most samples studied evidence recrystallization of sphalerite that is broadly coeval with formation of fluorite.

Involvement of sulfate-reducing bacteria in the formation of this early sphalerite mineralization is supported by sulfur isotope data. Sphalerite is generally characterized by isotopic light sulfur with δ^{34}S per mil values ranging from –30.5 to –20.3 per mil. The most negative sulfur isotope values are recorded from sphalerite (–30.5‰, –30.2‰) and galena with unusual fibrous to dendritic morphology (–31.9‰; –31.8‰); both are associated with oxysulfides. Microglobular sphalerite with well-preserved sphalerite globules has a δ^{34}S value of –28.8 to –28.2 per mil; colloform sphalerite (schalenblende) ranges from –29.0 to –25.0 per mil. Microglobular sphalerite associated with fine-grained fluorite and euhedral sphalerite formed through recrystallization processes show a trend to less negative values; i.e., –26.3 to –22.2 per mil and –22.9 to –20.3 per mil, respectively. We suggest that the combined biogenic nano- to macrotextures and sulfur isotope data are evidence that microbes played a key role in formation of Alpine carbonate-hosted Zn-Pb deposits. Results of this study contradict the MVT model suggested for Alpine Pb-Zn deposits, which calls for formation of Pb-Zn mineralization during late diagenetic burial in the Late Triassic-Early Jurassic.

Introduction

Strata-bound, carbonate-hosted Pb-Zn deposits are a major subclass of sediment-hosted Pb-Zn deposits (e.g., Sangster, 1996; Leach et al., 2005). These low-temperature (<200°C) Pb-Zn deposits occur in crustal settings, most commonly in carbonate-dominated platform sequences of Phanerozoic age, and are often collectively lumped together as Mississippi Valley-type (MVT) deposits (e.g., Leach et al., 2005). However, there is little consensus on the classification of these deposits and the assignment of some of them to the MVT subclass is not generally accepted, especially because the timing of mineralization with respect to the depositional age of the sediments is unknown for many of them. There is also no consensus on to what extent sedimentary exhalative processes contributed to the formation of these deposits (Evans, 1993). This is especially true for some of the Irish (e.g., Navan) and Alpine (e.g., Bleiberg; Schroll, 1997) examples.

One neglected aspect in the study of carbonate-hosted Pb-Zn deposits is the role of microbial processes in their formation, a topic that started to attract the general interest of economic geologists only recently (e.g., Southam and Saunders, 2005). Most evidence for the involvement of microorganisms in the formation of carbonate-hosted Pb-Zn deposits is based on sulfur isotopes. Strongly negative sulfur isotope compositions of sulfides are commonly regarded as evidence for BSR (e.g., Fallick et al., 2001; Bawden et al., 2003). Microtextural evidence for the involvement of bacteria in the mineralization process is rare. Sulfide microglobules interpreted as biogenic peloids have, however, been reported from carbonate-hosted Pb-Zn deposits in Ireland (Kucha, 1988; Kucha et al., 1990) and the Upper Silesian MVT deposits in Poland and Belgium (Kucha and Viaene, 1993).

In this study we present nano- to macrotextural and sulfur isotope evidence supporting the hypothesis that microorganisms

†Corresponding author: e-mail, johann.raith@unileoben.ac.at
°Deceased, February 24, 2008

Submitted: July 19, 2009
Accepted: May 19, 2010

played a major role in formation of the Bleiberg deposit, the largest Pb-Zn deposit in the Alps. The textural interpretations are supported by microanalytical data and a set of new sulfur isotope data.

Geologic Setting

The Bleiberg Pb-Zn mining district is located in the Drau Range, about 10 to 20 km east of the town of Villach in Carinthia, Austria (Fig. 1). Bleiberg and several other major Pb-Zn deposits in this region—Windisch-Bleiberg, Obir, Mezica (Mieß, Slovenia), Cave di Predil (Raibl, Italy), and Salafossa (Italy), now all abandoned—are hosted by Triassic platform carbonates of the Carnian stage (Cerny, 1989a, b; Schroll, 1997; Leach et al., 2003). Smaller Pb-Zn deposits also occur in the Anisian stage. All of these Pb-Zn mines occur in close vicinity to the Periadriatic lineament, a major tectonic structure in the Alps separating the Eastern from the Southern Alps (Fig. 1). Bleiberg is the largest of these deposits, and until its closure in 1993 it produced 2.2×10^6 t of combined Zn and Pb, as well as 993 t Cd and 172 t Ge (Schroll, 2006).

The Drau Range is the southernmost part of the tectonically highest Upper Austroalpine cover sequences in the Eastern Alps (Fig. 1). It is composed of 4- to 5-km-thick Permomesozoic sediments, which were deposited on metamorphic basement rocks (Gailtal Crystalline Complex, Carboniferous of Nötsch, Fig. 2). After the deposition of Permoscythian red beds and Anisian shallow marine carbonates, Ladinian to Carnian carbonate platform sediments of the Wetterstein Formation were deposited. Cyclothemes are of special relevance in the Wetterstein Formation. They developed in a shallow-marine lagoonal facies in a paleotopographic high ("Sonderfazies," "Bleiberg facies," "Erzkalk"). Sedimentation in this special sedimentary environment was interrupted by emersion periods, causing formation of unconformities, karstification, and resedimentation (Bechstaedt, 1975a). Evaporites are also common in this sequence. The majority of the strata-bound Pb-Zn orebodies of the Erzkalk horizon are located in the upper 120 m of this special facies of the Wetterstein Formation (see below, Fig. 2).

Stratigraphically above the Wetterstein Formation are carbonatoclastic sediments of the Carnian Raibl Group, lagoonal dolomites of the Norian Hauptdolomite Formation, and basinal shales of the Late Norian to Rhaetian Kössen Formation. More details about the stratigraphy and facies differentiation in the Bleiberg area can be found in Cerny (1989b) and Zeeh and Bechstaedt (1994). Jurassic hemipelagic to Cretaceous flysch sediments, which were deposited in an oblique slip zone (Schmidt et al., 1991), are only preserved in the western Drau Range, not in its eastern part in the Bleiberg area.

The whole sedimentary pile reflects evolution of an unstable shelf at a passive continental margin of the Thetys (Early to Middle Triassic), followed by opening of the Meliata ocean (Late Triassic to Early Jurassic), and finally subduction of this ocean (Late Jurassic to Early Cretaceous) during the Alpine orogeny. Mesozoic north-to-south compression and subsequent Mesozoic to Neogene extension and strike-slip tectonics resulted in tectonic folding, thrusting, and intense fragmentation of the Drau Range and its Pb-Zn deposits (see summary in Rantitsch, 2001). The most prominent are east-west–trending, steep to subvertical normal and strike-slip faults, which are the dominant tectonic feature in the eastern part of the Bleiberg deposit (e.g., Cerny, 1989b). However,

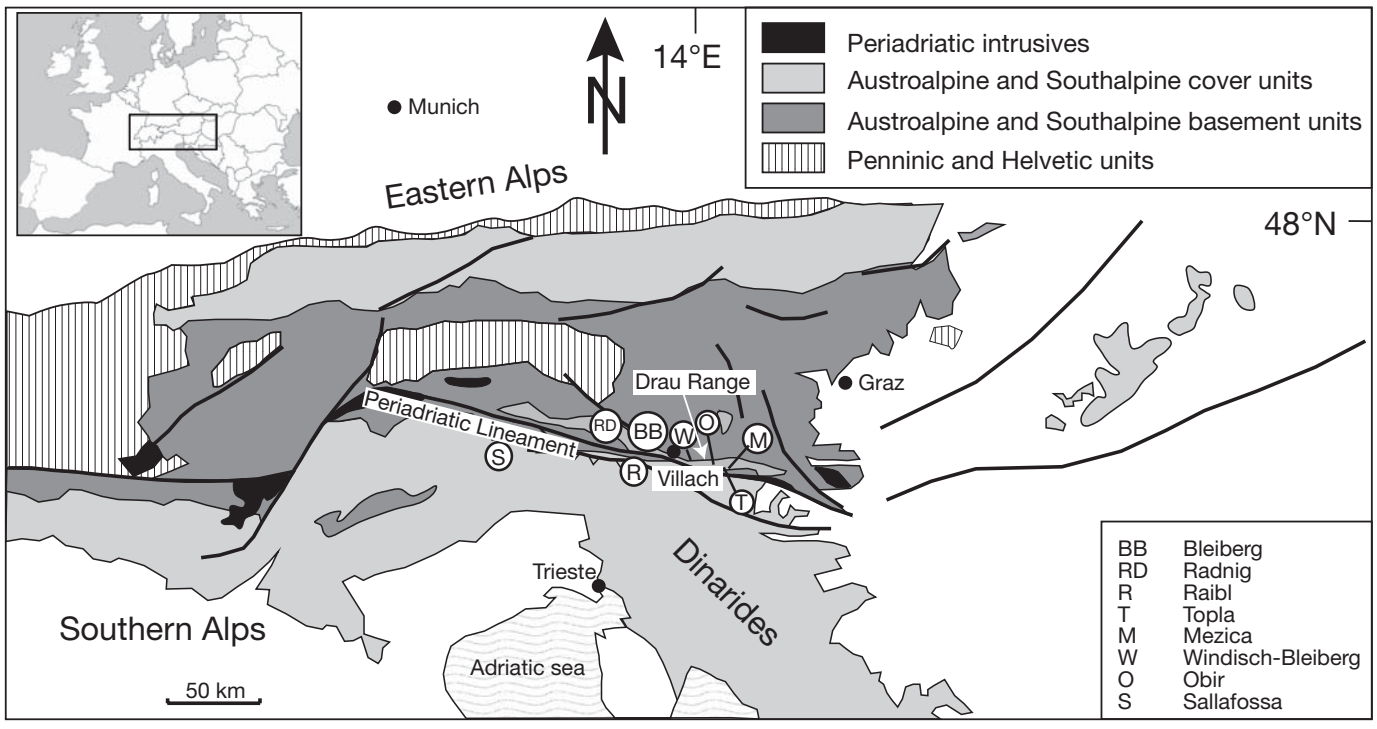

FIG. 1. Geologic sketch map showing the main units in the Eastern Alps and location of major carbonate-hosted Pb-Zn deposits in the Drau Range and to the south of the Periadriatic lineament (from Schroll and Rantitsch, 2005, modified). Inset map shows geographic location of map in Europe.

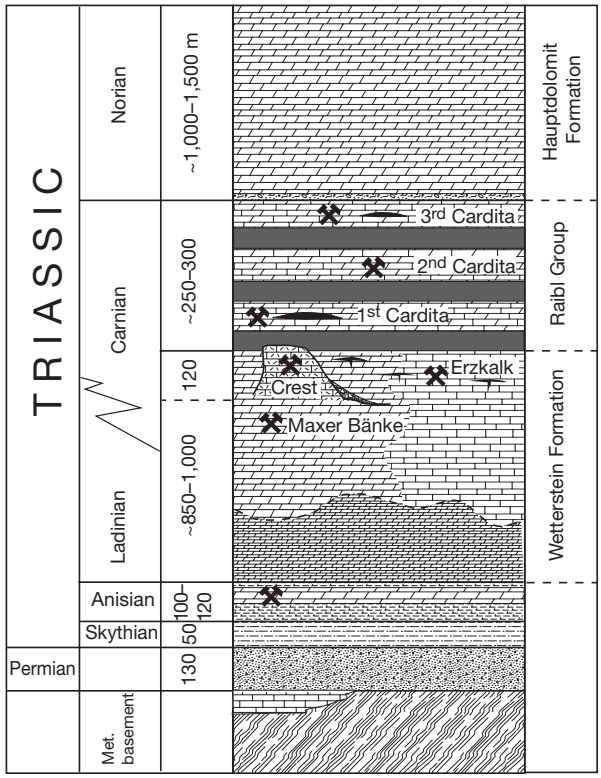

FIG. 2. Schematic stratigraphic profile of the Bleiberg Pb-Zn deposit showing the six main ore horizons (Maxer Bänke, Erzkalk, Crest, first to third Cardita) in the Carnian Wetterstein Formation and Raibl Group (from Cerny, 1989a, simplified).

not all these faults are postdepositional; some of them and the associated breccias already formed during sedimentation in the Middle Triassic (Schulz, 1975).

Based on vitrinite reflectance data and one-dimensional thermal modeling, Rantitsch (2001) reconstructed the thermal history of the Drau Range. He distinguished three thermal events: (1) heating due to basin subsidence (characterized by low heat flow of 60 mW per m^2), (2) local heating due to Oligocene magmatic intrusions along the Periadriatic lineament, and (3) highly elevated posttectonic heat flow in the central northern part of the Drau Range due to uplift of the Tauern dome in the Early-Middle Miocene. Vitrinite reflectance values for the Carnian Raibl Group in the eastern Drau Range near Bleiberg range from 0.7 to 1.0 percent and are correlated with the heating during basin subsidence.

Reevaluation of fluid inclusion data with the thermal model for the Drau Range suggests maximum burial temperatures of 130° to 150°C for the Carnian platfom carbonates and 190°C for the Permoscythian clastic sediments at the base of the Drau Range basin, respectively (Rantitsch, 2003). Maximum burial was reached in the Late Cretaceous-Early Tertiary. In contrast, the Late Triassic Carnian strata that host the Pb-Zn deposits were buried to ~3 km depth and heated up to not more than ~120°C (Rantitsch, 2003).

Igneous rocks are very rare in the stratigraphic sequence. A few thin tuff layers are intercalated in the stratigraphic sequence (e.g., in the Anisian Muschelkalk and in the Maxer Bänke horizon; Cerny, 1989b). Intercalations of green dolomitic marls in the latter (associated with black breccias) were interpreted as either pyroclastic material (Schneider, 1964) or as residual weathering products (Bechstaedt, 1975a). No intrusive rocks are known from the Drau Range except a few mafic dikes of Oligocene age. Larger intrusions emplaced along the Periadriatic lineament and associated faults in the Oligocene did not cause any thermal effects in the eastern Drau Range (Rantitsch, 2003).

Six stratigraphically definable ore horizons have been distinguished at Bleiberg (Fig. 2):

1. The Erzkalk horizon, consisting of 15 strata-bound Pb-Zn orebodies in limestone in the top 120 m of the special lagoonal facies of the Wetterstein Formation (see above). These strata-bound orebodies (concordant ores and discordant-fissures) were the main targets of mining for about 700 years (Cerny, 1989b).
2. Maxer Bänke horizon, another strata-bound Zn-Pb zone in dolostone and dolomitic and marly limestones in the middle part of the Wetterstein Formation, representing the stratigraphically deepest ore horizon.
3. Crest horizon ("Schwellenfazies"), an irregular, partly breccia-dominated, high-grade Zn-rich body in massive dolomitized limestone of the upper Wetterstein Formation.
4–6. Three Cardita horizons, all of which are strata-bound Pb-Zn orebodies in carbonate rocks of the Raibl Group, separated by three ~20-m-thick shale horizons (first, second, and third Cardita shale). In addition, subeconomic Pb-Zn mineralization is hosted in Anisian carbonate rocks in the Drau Range; the largest of these Anisian deposits is located at Topla near Mezica in Slovenia (Figs. 1, 2). For more details, the reader is referred to the review papers (with references therein) by Schroll (1997, 2006, 2008).

Materials and Methods

This study focused on samples from the Crest (17 samples) and the first Cardita (15 samples) horizons. Because most parts of the abandoned Bleiberg mine are currently inaccessible, the study had to rely on sample material collected by E. Schroll before closure of the mine in 1993. Additional samples were provided from the mineral collections of the University of Leoben and the Ludwig-Maximilians-Universität Munich, as well as from private collections.

Polished sections were studied by reflected light microscopy. Samples were polished with diamond spray, using light oil as a lubricant. This enabled the preservation of water-soluble minerals (chlorides and oxysulfides) in the polished sections. Samples for sulfur isotope analyses were obtained by drilling of selected microareas on polished sections using the Ulrike Medenbach microdrill system mounted on an Olympus BX40 microscope.

Sulfur isotope measurements were performed at the Mass Spectrometry Laboratory, Institute of Physics, UMCS, Lublin, Poland. The quantity of sample volume varied from 1 to 3 mm^3, equivalent to 4 to 10 mg. Samples were oxidized to SO_2 with Cu_2O (Robinson and Kusakabe, 1975), separated from CO_2 cryogenically, and the SO^+ spectrum (m/z = 48 and 50 peaks) was analyzed. The standard uncertainty (1σ standard deviation) of the $\delta^{34}S$ values is 0.05 per mil.

Electron microprobe WDS analyses were performed at the Department of Applied Geosciences and Geophysics, University of Leoben, with an ARL SEMQ instrument at 20 kV and a probe current of 120 μA, equivalent to a sample current of 10 to 14 nA, using the following spectral lines and standards (in parentheses): SK_α, FeK_α and CuK_α (FeS_2, $CuFeS_2$), MnK_α ($MnCO_3$), NiK_α (NiS), ZnK_α ($Zn_{0.8889}Fe_{0.1110}S_1$), AsL_α (FeAsS), CdL_α, AgL_α, TlM_α (lorandite, $TlAsS_2$), PbM_α (PbS), and ClK_α (tugtupite). The Bastin data reduction procedure has been used. Relative analytical uncertainty (2σ) of the analyses is about 1 percent of the measured value. To avoid matrix effects when analyzing small inclusions (e.g., carbonate inclusions in sphalerite), the minimum size of the inclusions measured was 10 μm.

Sulfur valences were determined with the same instrument, using a PET crystal by measuring the peak shifts of the SK_α and SK_β lines (Kucha et al., 1989). Cubic FeS_2 was measured as a reference (S valence = –1 and 0) before and after a given unknown. Peak position has been measured 5 to 7 times, and these measurements were used to calculate the standard deviation, which in turn has been used to establish the accuracy of valence determination. Fine scans of the SK_α and SK_β peak top were performed using a PET crystal, applying two motor step units with dwell time equal to 4 s. Oxygen content was measured with a CAMEBAX microprobe at the Faculty of Material Sciences, Krakow, Poland at 10 kV, using Fe_2O_3 as a standard.

To reveal possible bacterial microtextures, polished samples were etched with a 1:1 molar mixture of $KMnO_4$ + H_2SO_4 for 12 min (sphalerite), saturated solution of EDTA for 3 to 30 min (calcite, Zn-calcite), and 0.1n HCl for 2 to 6 min (dolomite). Secondary electron imaging of micro- and nanotextures was performed on these etched, polished sections with a Hitachi S-4700 field emission scanning electron microscope (FESEM) with cold cathode at the Institute of Geological Sciences, Jagiellonian University, Krakow. This instrument allows effective magnification of 500,000 times with an excellent resolution of nanotextures.

Sphalerite Textures

Macro- and microtextures of sulfides

Sulfides display characteristic macro- to microtextural features. Finely banded, semimassive sphalerite, with colors of individual bands varying from yellowish to dark brown in hand specimen, is characteristic for these ores. The thickness of individual sphalerite bands varies from 0.5 to 3 mm, and their lateral extension may be up to 5 cm (Fig. 3A). They often form discontinuous, wavy to ripped-up layers of fine-grained sphalerite (Fig. 3B).

Several bands-microareas can be distinguished in sample Bl-5 from the first Cardita horizon. For descriptive purposes, these are labeled with Roman numerals (Fig. 3A). Semi-massive to colloform sphalerite (schalenblende) layers alternate with carbonate- and marcasite-rich layers and discontinuous, wavy bands of grayish color (Fig. 3A, microareas I, IV); in the latter, spherules and bands of colloform pyrite intergrown with oxysulfides are found in addition to sphalerite microglobules and organic matter (Fig. 4A, B). The globular morphology of sphalerite embedded in the silicified clay-organic matrix is

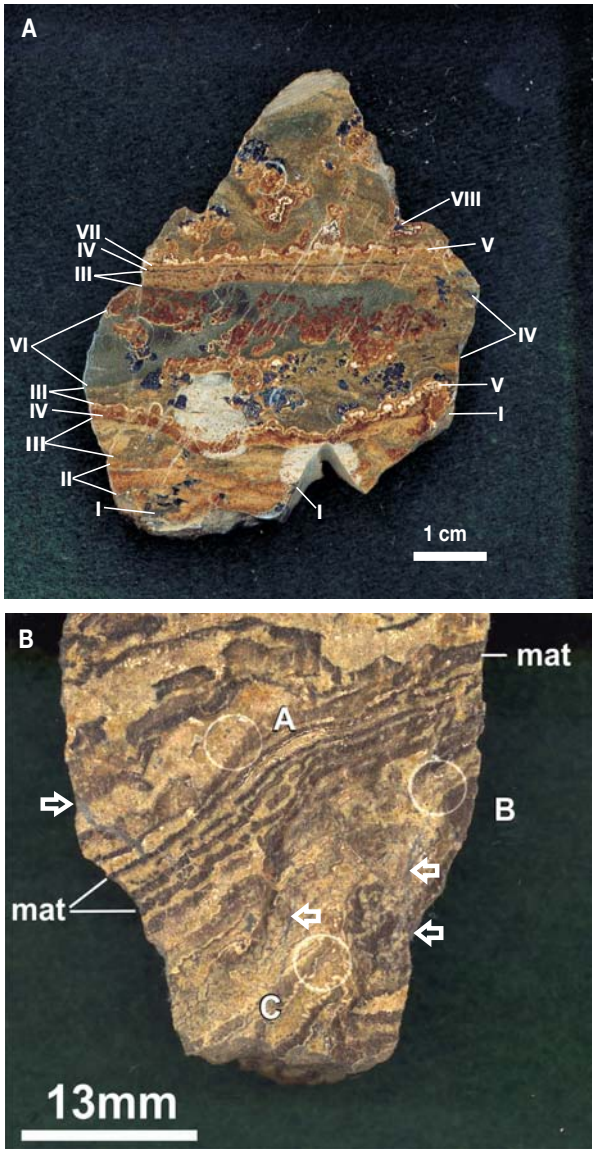

FIG. 3. (A) Photograph of hand specimen from the first Cardita horizon showing rhythmically banded to chaotic sulfide textures:. Roman numerals (I–VIII) indicate the different microareas analyzed and referred to in the text and Table 6. (I) Microglobular sphalerite in gray silicified clay matrix, for details see Fig. 4A, $\delta^{34}S$ = –28.8 per mil; (II) semimassive brownish sphalerite partially or entirely replacing microglobular sphalerite, $\delta^{34}S$ = –26.5 per mil; (III) carbonate matrix with variable amounts of microglobules replaced by sphalerite, for details see Fig. 4E, $\delta^{34}S$ = –22.2 per mil; (IV) thin gray layer composed either of microglobules of sphalerite or Fe oxysulfides (for details see Fig. 4B), $\delta^{34}S$ = –30.2 per mil; (V) colloform sphalerite (reddish brown to whitish schalenblende) overgrowing microglobular sphalerite, $\delta^{34}S$ = –29.2 per mil; (VI) variably thick layer (gray-green) of fine-grained, euhedral marcasite with oxysulfide relicts, $\delta^{34}S$ = –26.0 per mil; (VII) thin porous layer of microglobular sphalerite forming base of colloform sphalerite layer, $\delta^{34}S$ = –26.3 per mil; (VIII) dendritic fibrous PbS and sphalerite after oxysulfide precursor, $\delta^{34}S$ = –31.80 per mil. Whitish, light gray patches in lower part of photo are artifacts due to etching. Specimen Bl-5 from the mineralogical collection of the Department of Applied Geosciences and Geophysics, University of Leoben. (B) Photograph of massive sphalerite ore from Crest horizon composed of two sphalerite types—one, light brown, forming the matrix, and the other, dark brown, forming discontinuous, 0.5- to 3.5-mm-thick, broken-up layers are interpreted as former microbial mats ("mat"; see discussion). Gray fractures (arrowed) are filled with secondary anhydrite. A, B, C circles where microscopic pictures were taken (Fig. 4C) and where analyses were made. Sample Bl-21 from collection Mosser, Antoni West 8th level.

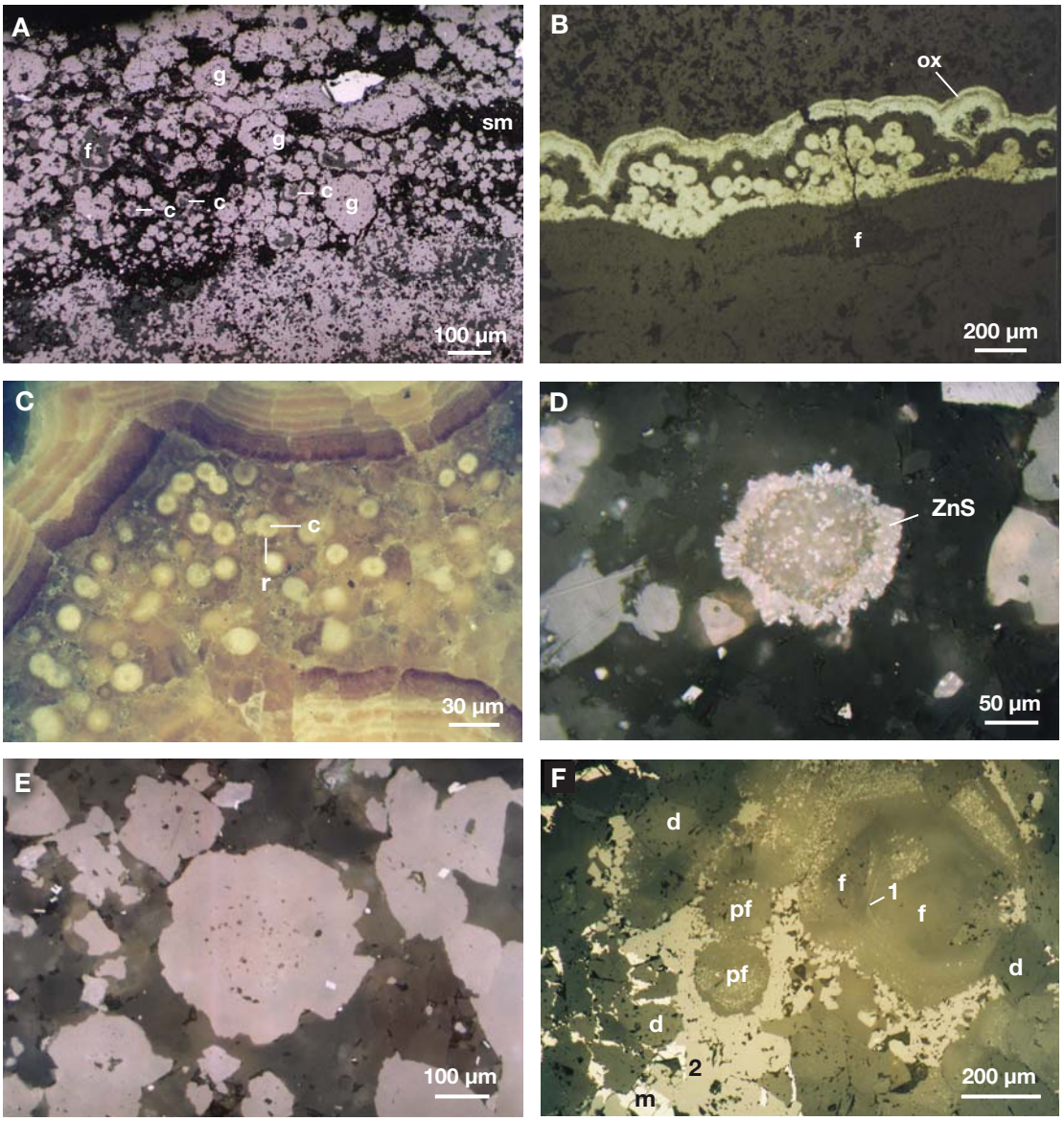

FIG. 4. (A) Photomicrograph of ~5-mm-thick layer composed mainly of sphalerite microglobules (light gray, g) in silicified matrix (sm) of argillaceous-carbonaceous material. Some globules preserve dark gray carbonate cores (c). Some fluorite (medium gray, f) is also present. Bottom of photograph shows very fine grained angular sphalerite with grain sizes from 1 to 25 μm coalescing into larger, globular-to-ovoid sphalerite aggregates (g). Reflected light, sample Bl-5, first Cardita horizon. Detail of microarea I shown in Figure 3A. (B) Photomicrograph of wavy bands and spherules of pyrite (bright yellowish) - oxysulfide (ox, darker bands) in banded sphalerite matrix (dark gray) containing some fluorite (f); pyrite oxysulfide layer has δ^{34}S = –30.2 per mil, sphalerite above has δ^{34}S = –26.3 per mil, and sphalerite below has δ^{34}S = –30.5 per mil. Reflected light; sample Bl-5, first Cardita horizon. Detail of microarea IV shown in Figure 3A. For sulfur isotope data, also see Table 6. (C) Photomicrograph of sphalerite band containing numerous circular to ovoid microstructures, which are composed of darker cores (~25–55 μm, c) and light-colored rims (~10–30 μm, r). The layers above and below are finely banded colloform sphalerite. The layer with the circular to ovoid structures is interpreted as a former peloid-rich microbial mat. Reflected light, crossed polars; sample Bl-21 from collection Mosser, Crest horizon; detail of area C shown in Figure 3B. (D) Photomicrograph of composite carbonate-sphalerite microglobule interpreted as a peloid. The darker core is composed of Zn dolomite (confirmed by EDS), with numerous higher reflecting μm-size sphalerite inclusions and surrounded by a serrated sphalerite rim (bright, internal reflections, 10–35 μm thick). The matrix is dolomite (dark-gray) and also contains angular sphalerite crystallites, 1 to 30 μm in size. Reflected light; sample Bl-4, first Cardita horizon. (E) Photomicrograph of sphalerite microglobule (light gray, center of photo) composed of a core with numerous up to 20-μm inclusions of Zn calcite (dark gray; analyses A1 in Table 1) and inclusion-free sphalerite rim (except for rare marcasite rhombs, white). The globule is set in a calcite matrix containing small inclusions of angular sphalerite with grain size from 1 to 30 μm. Reflected light; sample Bl-4, first Cardita horizon. (F) Photomicrograph of complex microtexture represented by (i) microglobules now replaced by fluorite. The globules contain minute inclusions of sphalerite and are interpreted as former bacterial peloids (pf), (ii) large fluorite crystal showing complex internal growth zoning. Individual growth zones within the crystal are outlined by fine-grained sphalerite trails (1), (iii) sparry dolomite (d), (iv) coarser-grained sphalerite (2) partly preserved as rims around the microglobules, and (v) marcasite (m) filling up interstitial spaces between dolomite and sphalerite. Reflected light; sample 43, Maxer Bänke horizon.

much better preserved (Fig. 4A, center to top part), compared to that in the carbonate matrix (Fig. 4A, lower part). Globules in the carbonate matrix are composed of agglomerations of individual sphalerite grains, from a few nanometers to a few μm in size. Individual sphalerite microglobules are from 40 to 90 μm diameter (Fig. 4A). Some wavy layers are composed of pyrite-oxysulfide-sphalerite intergrowths with a banded to globular morphology. The intergrown phases can be distinguished by their different reflectivity (R) in reflected light (R = 54% in pyrite down to about 17% in oxysulfide; Fig. 4B). The microglobules show cores composed of pyrite, oxysulfides, or sphalerite (Fig. 4B). The bands and the microglobules are composed of fine-grained acicular crystallites forming spherulitic radial crystal aggregates. Oxysulfides are commonly replaced by more stable sphalerite or galena (for details, see Kucha and Stumpfl, 1992).

In massive sphalerite ore from the Crest horizon (Fig. 3B), the grayish, wavy, disrupted bands mainly consist of masses of spherical to ovoid sphalerite. Individual microglobules are composed of lighter cores and distinct darker coronas, best seen under crossed polars in reflected light (Fig. 4C). The diameter of the cores varies from 10 to 50 μm, the thickness of the rims (coronas) varies from 10 to 30 μm. Thus, the overall dimension (core + corona) of these sphalerite microglobules varies from 20 to 80 μm. The core is composed of Zn-rich calcite plus rod-like sphalerite filaments. In places, the calcite core can be partly replaced by fluorite. The corona is composed of sphalerite.

Composite sphalerite globules are also preserved as clumps in the matrix (Fig. 4D, E) showing various stages of transformation into bigger sphalerite globules. During subsequent transformation, the cores, 60 to 70 μm in diameter, composed of Zn-rich calcite or Zn-rich dolomite (Table 1) and surrounded by a thin (20–30 μm) sphalerite corona (Fig. 4D), become successively replaced by sphalerite (Fig. 4E). Numerous minute carbonate inclusions, from a few to 25 μm in size, are preserved in the former cores. Due to this replacement and accompanying recrystallization the size of the sphalerite globules increases up to 100 to 180 μm and the globules become increasingly distorted. In addition to the sphalerite microglobules, 5- to 25-μm large, angular sphalerite crystals, often with sub- to euhedral crystal shape, are embedded in the calcite matrix (Fig. 4D, E).

Locally, fluorite is observed in amounts varying from traces to a few vol percent. Fluorite is present in the following, varied forms: (1) as finely dispersed fluorite replacing micritic calcite, (2) as replacement of calcite that is present in cores of composite microglobules (Fig. 4F), (3) as replacements of the former fibrous Zn-calcite or Fe-smithsonite within banded sphalerite, and (4) as fracture infillings together with blue anhydrite (Fig. 3B). Coarser-grained dolomite cement postdates formation of microglobular sphalerite and its replacement by fluorite (Fig. 4F); coarser angular sphalerite coexists with this blocky cement.

Nanotextures

After etching, sphalerite microglobules are spotted with microcavities that formed from dissolution of Zn calcite (Fig. 5A). Rare microfilaments about 1 μm long, and numerous nanospheres (20–70 nm) become visible under high magnification in the etched cavities (Fig. 5B, C). These microfilaments and nanospheres are identical to those previously documented from the Crest horizon (Kucha et al., 2005). Larger sphalerite microglobules, 100 to 180 μm in diameter and without direct spatial connection to filamentous forms, are also present. Microfractures in these globules are filled with

TABLE 1. Chemical Composition (wt %, Moles) of Calcite and Dolomite Determined by Wavelength Dispersive Electron Microprobe Analyses, Bleiberg Pb-Zn Deposit

Sample no.	CaO	MgO	FeO	MnO	ZnO	S	Comments
Bl4A1	55. 40	0.18	0.05	≤0.01	2.09	0.003	Inclusion (>10 μm) in replaced
	0.970	0.004	0.001		0.025		microglobule, core
Bl21eC4	55.96	0.20	0.08	≤0.01	2.69	0.04	Inclusion (>10 μm) in replaced
	0.962	0.005	0.001		0.032		microglobule, core
7A2	30.76	20.30	0.07	0.03	2.51	0.07	Inclusion (>10 μm) in replaced
	1.012	0.928	0.002	0.001	0.057		microglobule, core
7A5	30.67	21.56	0.01	≤0.01	0.64	0.08	Carbonate matrix
	1.004	0.981	0.000		0.014		
7E2	55.36	0.15	0.01	≤0.01	2.21	0.05	Inclusion (>10 μm) in euhedral
	0.996	0.004	0.000		0.027		sphalerite
7E3	56.81	0.12	0.02	≤0.01	0.60	0.02	Carbonate matrix
	0.990	0.003	0.000		0.007		
9A4	54.45	0.11	0.04	≤0.01	0.51	0.03	Carbonate matrix
	0.990	0.003	0.001		0.006		
9A5	54.01	0.08	0.01	≤0.01	1.10	0.02	Carbonate matrix
	0.984	0.002	0.000		0.014		
18A3	55.50	0.20	0.01	≤0.01	3.04	0.08	Relict in semimassive ZnS
	0.959	0.005	0.000	0.000	0.036		
18E2	55.20	0.28	0.33	0.12	2.16	0.11	Cement of euhedral sphalerite
	0.961	0.007	0.005	0.002	0.026	0.003	
18E3	30.65	20.88	0.12	≤0.01	1.46	0.03	Interstitial between euhedral sphalerite
	1.008	0.956	0.003		0.003		
18E3a	30.90	20.80	0.02	≤0.01	0.51	0.02	Interstitial between euhedral sphalerite
	1.034	0.968	0.001		0.012		

The upper line for each sample gives the wt %, the lower one the moles

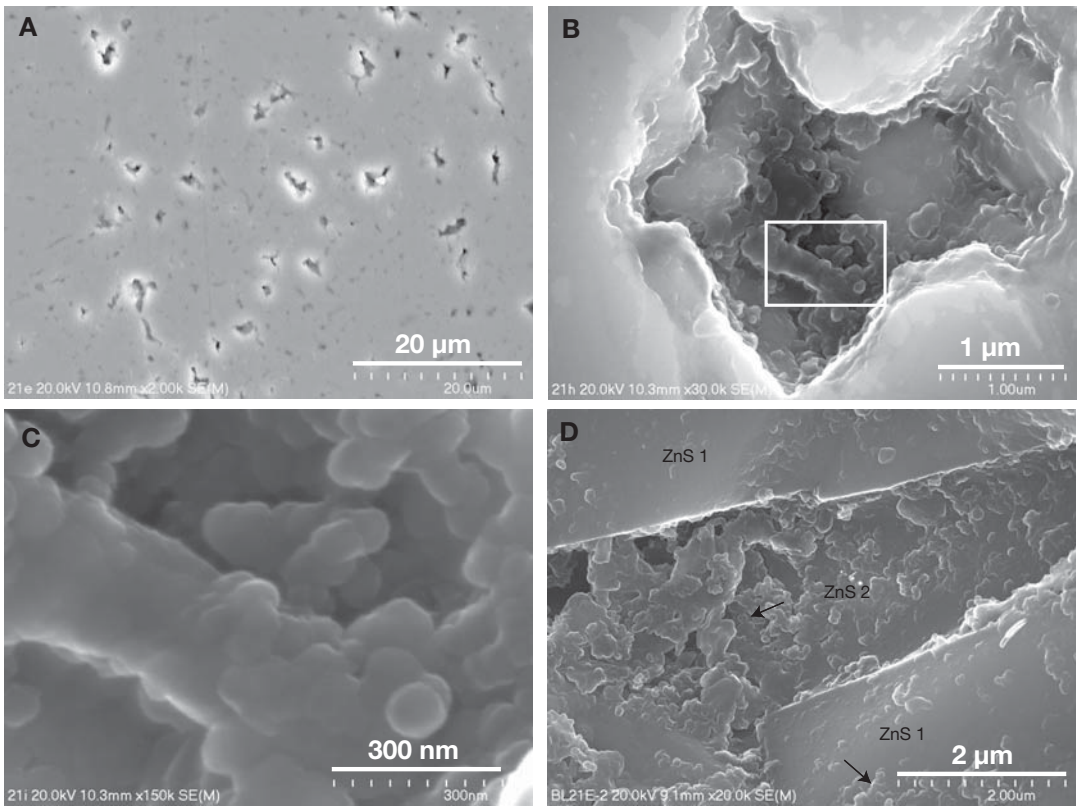

FIG. 5. (A) FESEM image of sphalerite microglobule (gray) containing numerous voids (dark) left over after dissolution of calcite inclusions by etching. Sample Bl-21 microarea C (see Fig. 3B), Crest horizon, Antoni West 8th level. (B) FESEM image of etched cavity within a sphalerite microglobule that was filled with calcite before etching revealing numerous nanoscale spherical forms with size from 20 to 90 nm. Cavity walls are also composed of tiny, coalesced sphalerite spheres building up the entire sphalerite globule measuring 120 μm. Boxed area is shown in Figure 5C. Sample Bl-21 microarea C (see Fig. 3B), Crest horizon, Antoni West 8th level. (C) FESEM image of boxed area in Figure 5B showing individual sphalerite nanospheres ranging in size from 15 to 90 nm and a part of a mineralized bacterial filament. (D) FESEM image showing details in a microfrature cutting a 150-μm, large sphalerite microglobule. The microfracture is filled with coalesced sphalerite nanospheres (arrow, ZnS 2). The older recrystallized sphalerite, cut by the fracture, is also composed of relics of coalesced sphalerite nanospheres (arrow, ZnS 1). Sample Bl-21, Crest horizon, Antoni West 8th level.

nanospheres ranging from 5 to 90 nm; both the older sphalerite accumulations ("ZnS 1") as well as later infillings in microfractures ("ZnS 2") are composed of spherical nanoforms (Fig. 5D).

Another nano- to microtexture common in the fine-banded first Cardita ore (sample Bl-5) is framboidal pyrite (Fig. 6A). It forms spherical agglomerations about 7 to 10 μm size that are composed of euhedral pyrite crystals measuring about 0.5 μm. In addition, there are 3 μm clumps composed of FeS_2 nanospheres about 30 nm in diameter (Fig. 6B); the latter are best preserved in the silicified clay matrix (Fig. 6B). Enveloping sheaths of clay minerals often blur the outline of the nanospheres. Rarely, grains of framboidal sphalerite occur together with microglobular sphalerite (Fig. 6C).

Mineral Chemical Compositions

The texturally different types of sphalerite distinguished in this study show remarkable differences in trace element composition (Table 2). Cores of sphalerite microglobules (interpreted as peloids; see below) are enriched in Fe (avg 1.68 wt %; Table 2) compared to all other sphalerite types, which have lower Fe contents. Cores of larger globular sphalerite aggregates have slightly higher Fe contents (avg 0.39 wt %) compared to sphalerite coronas-rims or euhedral sphalerite,

TABLE 2. Iron and Cd Contents (wt %) of Sphalerite Determined by Wavelength Dispersive Electron Microprobe Analyses, Bleiberg Pb-Zn Deposit, Sample Bl-4, 1st Cardita Horizon

ZnS type	*n*		Fe	Cd
Microglobular ZnS	8	Avg	1.68	0.14
(peloids), core		Min	0.41	≤0.01
		Max	3.22	0.35
Microglobular ZnS	10	Avg	0.29	0.24
(peloids), corona		Min	0.04	≤0.01
		Max	0.64	0.39
Globular ZnS	6	Avg	0.39	0.21
aggregates, core		Min	0.06	0.09
		Max	0.96	0.39
Globular ZnS	6	Avg	0.23	0.18
aggregates, rim		Min	0.10	0.13
		Max	0.29	0.22
Angular (euhedral)	11	Avg	0.05	0.25
ZnS, 1–25 μm in size		Min	≤0.01	≤0.01
		Max	0.20	0.40

n = number of analyses

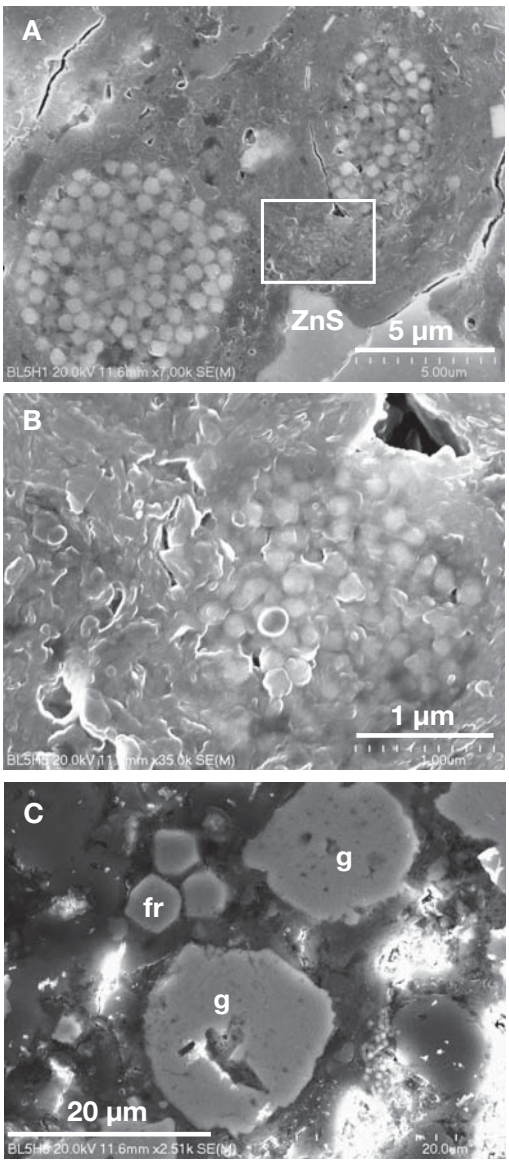

FIG. 6. (A) FESEM image of two microglobular agglomerations of Zn-bearing pyrite framboids from the silicified matrix of microarea I in Figure 3A. Box encompasses an area where nanoglobular FeS_2 aggregates are preserved (see Fig. 6B). Sample Bl-5; first Cardita horizon, Antoni. (B) FESEM image of boxed area in Figure 6A showing details of a ~3-μm, large spherical clump composed of ~30-nm FeS_2 spheres. The nanospheres are richer in Zn than micron-sized spheres composing the framboidal pyrite (see Table 3). The outline of nanospheres is slightly obscured by clay sheaths. Sample Bl-5, 1st Cardita horizon, Antoni. (C) FESEM image of framboidal sphalerite (fr) enriched in Fe and sphalerite nanoglobules (g). Sample Bl-5, first Cardita horizon, Antoni.

although there is a considerable overlap in Fe contents among these types (Table 2). Cadmium shows a reverse trend to Fe; angular euhedral sphalerite and coronas have higher Cd contents than the cores (Table 2).

Chemical compositions of carbonate minerals are listed in Table 1. Carbonate inclusions in microglobular sphalerite are from a few to 25 μm in size (Fig. 4E) and are either calcite or dolomite, containing 2.09 to 2.69 wt percent of ZnO. To avoid contamination from the surrounding sphalerite matrix, only analyses of carbonate inclusions larger than 10 μm are provided in Table 1. Dolomite and calcite inclusions preserved in incompletely replaced microglobular sphalerite cores, and calcite relics in recrystallized euhedral and semimassive sphalerite, respectively, also have higher ZnO contents. These carbonate inclusions are about two to five times richer in ZnO than the enclosing carbonate matrix (0.51–1.10 wt % ZnO, Table 1). Calcite cement and interstitial dolomite material of euhedral sphalerite have 2.16 and 1.46 wt percent ZnO, respectively. Sulfur concentrations are too low to balance Zn, and this suggests that Zn is bound to the calcite or dolomite lattice and that the higher Zn concentrations analyzed are not an artifact of the surrounding sphalerite matrix (Table 1). FeO and MnO contents are very low, mostly close to or below the detection limits of the electron microprobe.

Framboidal pyrite (Fig. 6A) contains 2.33 to 2.78 wt percent Zn (Table 3). All these analyses are high in SiO_2 and Al_2O_3, with some MgO and K_2O. These elements are from silicates (clay minerals?) intergrown with the framboidal pyrite. The μm-sized spherical clumps, made up of FeS_2 nanospheres (Fig. 6B), are wrapped in a clay material and the grains are too small to be analyzed separately. This explains the high SiO_2, Al_2O_3, MgO, and K_2O values in the analyses (Table 3). Neglecting these silicate-hosted elements and assuming that Zn is substituting for Fe, the composition of FeS_2 nanospheres deviates from ideal FeS_2. They have high Zn contents (2.68–3.56 wt %; Table 3) and the molar Fe-Zn ratios vary from 2.5 to 5.2. The excess in cations (Fe + Zn = 1.14–1.21, calculated on the basis of 2 sulfur atoms per formula unit) is either due to incorporation of some Fe (and Zn) in the intergrown silicate phases, or due to replacement of a primary thiospinel (e.g., greigite). Framboidal sphalerite (Fig. 6C) contains a few wt percent Fe (Table 3).

Oxysulfides contain significant admixtures of metals in addition to Fe (Table 4; wt %): Ni $\leq$0.03 to 3.39, As 0.05 to 6.03, Pb $\leq$0.04 to 3.89, and Zn $\leq$0.03 to 1.92. Oxygen contents (normally not analyzed, but assumed to be the difference to 100 wt %) are from $\leq$0.10 to 30.11 wt percent (Table 4). Oxygen contents were measured in sample 16B11 and 16B11a, however; they are 28.7 and 29.4 wt percent, respectively (Table 4). Some of these phases can be regarded as very impure pyrites containing significant oxygen; others are best referred to as Fe-oxysulfides (Table 4). Reflectivity (in air) of these phases varies in accordance with oxygen content. Analyses with low oxygen contents have the highest reflectivity (Table 4). The pyrite-Fe-oxysulfide phases contain sulfur with intermediate and mixed valences: S^{6+}, S^{3+}, S^{2+}, S^{2-}, and S_2^{2-} (Table 5). Observations in reflected light using high magnification and oil objectives show that these phases often are a mixture of very fine grains and/or fibers of optically different phases. This may explain some of the unusual chemical compositions shown in Table 4, e.g., analysis 16A2 (Table 4) shows a 1/2 S-O molar ratio, typical of trithionate, but the metal content is twice as high as in the trithionate formula.

However, some oxysulfide grains are homogeneous and large enough (20 $\times$ 35 μm) to determine more clearly their physical and chemical properties (Tables 4, 5; analysis 16B11, 16B11a). From their stoichiometry, the latter phase is likely a Pb-, Zn-bearing iron thiosulfate (Fe, Pb, Zn)S_2O_3 (Tables 4, 5). Its Pb and Zn contents vary from 1.38 to 1.64 wt percent and 1.66 to 1.70 wt percent, respectively (Table

TABLE 3. Chemical Composition of Framboidal Pyrite, Nanospherical FeS_2 Aggregates Associated with Framboidal Pyrite (See Fig. 6A, B), and Framboidal Sphalerite (See Fig. 6C) Determined by Wavelength Dispersive Electron Microprobe Analyses, Bleiberg Pb-Zn Deposit

Sample	Fe	Zn	S	Total	SiO_2	Al_2O_3	MgO	K_2O	
Bl-5 H1/1	37.84	2.34	42.75	100.26	10.33	4.17	1.49	1.34	Pyrite
	1.016	0.054	2.000						framboid
Bl-5 H1/2	40.09	2.78	46.53	98.49	5.58	1.58	1.48	0.45	Pyrite
	0.989	0.059	2.000						framboid
B l-5 H1/3	28.06	2.33	33.22	99.23	20.68	10.11	2.50	2.33	Pyrite
	0.970	0.069	2.000						framboid
B l-5 H1/4	30.77	2.54	36.38	99.70	17.36	8.60	2.23	1.82	Pyrite
	0.971	0.069	2.000						framboid
B l-5 H1/5	11.89	2.68	13.40	99.49	46.04	16.20	3.37	5.91	Nanospherical
	1.019	0.196	2.000						FeS_2 aggregate
B l-5 H1/6	10.67	3.31	13.26	98.70	46.21	16.71	3.02	5.52	Nanospherical
	0.924	0.245	2.000						FeS_2 aggregate
B l-5 H1/7	7.68	3.56	10.79	98.34	48.62	17.54	3.97	6.18	Nanospherical
	0.817	0.324	2.000						FeS_2 aggregate
B l-5 H2/1	4.11	63.09	32.80	100.81	≤0.01	≤0.02	≤0.02	≤0.04	Sphalerite framboid
	0.072	0.943	1.000						
B l-5 H2/1	3.78	63.50	32.11	99.39	≤0.01	≤0.02	≤0.02	≤0.04	Sphalerite framboid
	0.068	0.970	1.000						

The upper line for each sample gives the wt %, the lower one the number of Fe and Zn cations calculated on the basis of two (FeS_2) and one (ZnS) S per formula unit

TABLE 4. Chemical Composition of Oxysulfides Occurring in Banded Pyrite, Marcasite, and Galena Replacing Banded Oxysulfide Precursors, Bleiberg Pb-Zn Deposit: Results Obtained by Wavelength Dispersive Electron Microprobe Analyses

	Fe	Pb	Zn	Ni	Ag	As	S	∑	O $_{diff.}$	O $_{meas}$	R (%)[1]	Remarks
Bl1E1	45.25	2.71	1.21	≤0.03	0.50	0.13	38.21		11.92		24.70	Anisotropic
	4.080	0.066	0.124		0.023	0.009	6		3.752			
Bl1E3	45.72	0.30	1.92	0.04	≤0.03	0.08	27.14		22.38		18.3	Anisotropic
	5.835	0.005	0.174	0.004		0.006	5		8.263			
16A2	36.29	0.30	0.40	0.08	≤0.03	0.23	30.17		30.11		7.5	Trithionate?
	2.072	0.005	0.020	0.004		0.009	3		6.000			
Bl1E10	44.20	3.83	≤0.03	0.06	0.08	0.05	50.11		1.63		52.6	"Dirty" pyrite
	1.013	0.024		0.001	0.001	0.009	2					
23A1	38.96	≤0.04	0.30	3.39	≤0.03	6.03	50.83		0.49		51.2	"Dirty" pyrite
	0.880		0.006	0.073		0.102	2					
23B2	43.87	≤0.04	0.55	1.24	≤0.03	2.13	52.11		0.10			
	0.967		0.010	0.026		0.035	2					
BL2D5	33.53	3.89	1.83	≤0.03	≤0.03	0.35	35.67		24.73		9.0	
	1.081	0.034	0.050			0.008	2		2.779			
16B11	30.45	1.64	1.66	≤0.03	≤0.03	0.44	39.17	73.36	26.64	28.73	8.10	Thiosulfate
	0.893	0.013	0.042			0.010	2		2.726	2.940		
16B11a	31.12	1.38	1.70	≤0.03	≤0.03	0.67	38.78	73.65	26.35	29.37	8.50	Thiosulfate
	0.922	0.011	0.043			0.015	2		2.724	3.036		

The upper line for each spot gives the wt %, the lower one the number of cations calculated on the basis of the specified number of S; O $_{diff.}$ oxygen assumed by difference to 100 wt%; O $_{meas;}$ measured oxygen content

[1] R (%) reflectivity in air measured at a spectral wavelength of 550 nm

4). The average S valence in this compound is close to +2; there is a valence characteristic satellite peak at about 2463.6 eV, indicating sulfur +5 (Table 5; Fig. 7). Fine SK_β peak top scans suggest the presence of S^{1-}, S^0, and S^{5+} (Fig. 7). These different sulfur valences are expected in thiosulfate (Vairavamurthy et al., 1993). The EMPA analyses are accurate enough to determine the S valences (for details, see Kucha et al., 1989), thus allowing identification of this phase as thiosulfate. Pb-bearing thiosulfates were previously reported from carbonate-hosted Pb-Zn deposits (Kucha and Viaene, 1993). It seems that the admixture of Pb stabilizes thiosulfate and lowers or prevents its solubility in water.

Sulfur Isotope Data

Thirty-two new sulfur isotope analyses are listed in Table 6. They are shown together with previously published data (Schroll and Wedepohl, 1972; Schroll and Pak, 1983; Schroll and Rantitsch, 2005) in Fig. 8A, B. Most analyzed sphalerites are isotopically very light. The $\delta^{34}S$ values of sulfides from the 1st Cardita horizon range from –21.7 to –31.8 per mil, those from the Crest horizon ranges from –21.7 to –29.3 per mil, and those from other ore horizons from –8.3 to –22.9 per mil (Table 6).

Ten analyses of different microareas in sample Bl-5 (Fig. 3A) from the 1st Cardita horizon yielded values between –22.2

TABLE 5. Sulfur Valences Determined by Electron Microprobe in Oxysulfides Occurring in Banded Pyrite and Marcasite; Bleiberg Pb-Zn Deposit

Sample/ spot #	SKα eV	Valence	SKβ eV	Valence	Satellites	Valence by composition	Calc S^{6+}	Calc S^{5+}	Calc S^{3+}	Calc S^{2+}	Calc S^{2-}	Calc S_2^{2-}	Calc S^{1-}
Bl1E1	+0.28	+0.5	+0.42	+0.5	+6	+0.25	1.25				1.25	1.75	
Bl1E3	+0.75	+2.5	+0.57	+2.2	+6	+2.20	2.75				2.75	0.00	
16A2	+0.64	+1.9	+0.53	+1.9		+2.67							
	+0.81	+2.8	+0.69	+3.0	?	(+3, +2)			2.00	1.00			
Bl1E10	0.00	–1.0	0.00	–1.0	none	–1.0						2.00	
23A1	0.00	–1.0	0.00	–1.0	none	–1.0						2.00	
23B2	0.00	–1.0	0.00	–1.0	none	–1.0						2.00	
BL2D5	+0.56	+1.6	+0.04	–1.1									
			+1.38	+5.3	+6	+1.79	0.93				0.93	0.07	
16B11	+0.68	+2.0	+0.57	+2.0	+5	+2.0							
	±0.07	±0.22	±0.06	0.20		±0.15							
16B11a	+0.70	+2.0	0.60	+2.0	+5	+2.0							
	±0.08	±0.20	±0.05	±0.15		±0.10		1.00					1.00

and –31.8 per mil (Table 6). A layer of microglobular sphalerite, which is well preserved in the silicified clay matrix (microarea I in Figs. 3A, 4A) has –28.8 per mil, whereas a sphalerite band with relics of sphalerite microglobules yielded –26.5 per mil (microarea II in Fig. 3A). Layers composed of mixtures of fine-grained, microglobular sphalerite, calcite, argillaceous material, and fluorite (Bl-5 1a to c, microareas III and VII in Fig. 3A) have δ^{34}S values between –22.2 and –26.3 per mil. A layer of colloform sphalerite (schalenblende) lacking microglobular textures has a δ^{34}S value of –29.2 per mil (microarea V in Fig. A). Sphalerites containing relics of Fe oxysulfides also have very negative values of –30.2 and –30.5 per mil, respectively (microarea IV in Fig. 3A). A mixture of fine-grained galena with unusual fibrous to dendritic morphology and sphalerite, containing relics of oxysulfides (microarea VIII in Fig. 3A) yielded the most negative isotopic value of this study (δ^{34}S –31.8‰). Due to intergrowths of these phases, it was impossible to isolate them. Marcasite from the same sample has a δ^{34}S value of –26.0 per mil (microarea VI in Fig. 3A).

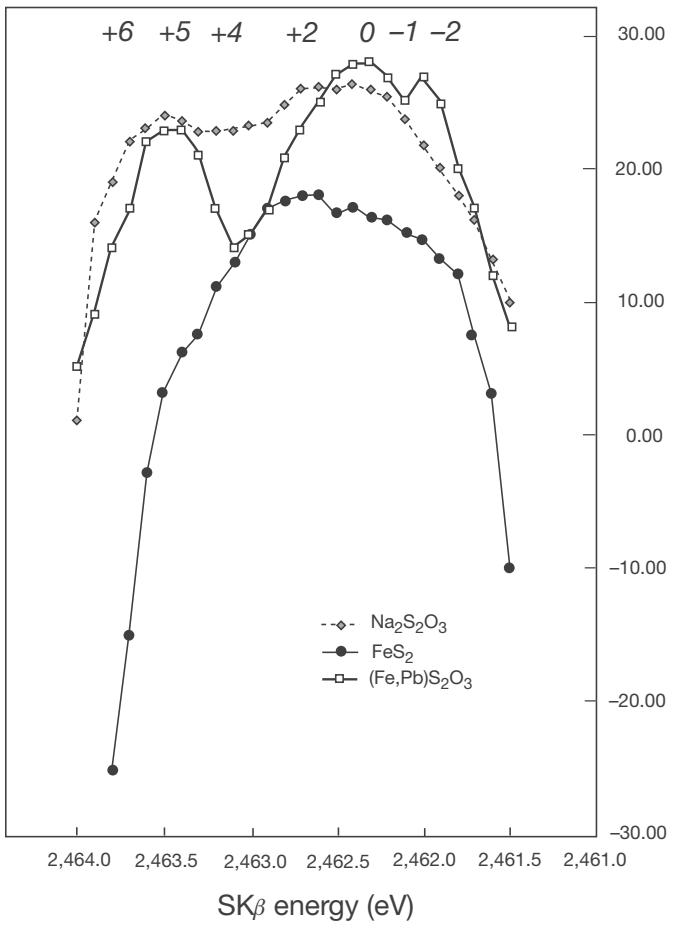

FIG. 7. Fine scan of the SKβ peak top showing resolved S valences: –1 and 0 in pyrite standard, –1 (and 0?) and +5 in thiosulfate standard (for detail of S valences in thiosulfates, see Vairavamurthy et al., 1993), and –1, 0, and +5 in the $(Fe,Pb)S_2O_3$ thiosulfate studied (Table 4; Samples 16B11, 16B11a).

Eight analyses were carried out on different microareas of sample Bl-21 from the Crest horizon (analyses Bl-21 A to H, Table 6). All samples, which are composed of massive coalesced sphalerite microglobules are quite negative, the δ^{34}S values varying from –27.8 to –29.3 per mil. A pure sphalerite layer containing about 35 to 40 percent microglobular sphalerite (Fig. 3B, 4C) has a δ^{34}S –27.9 per mil; sphalerite formed by intense replacement of sphalerite microglobules in the same sample has –28.21 per mil.

Less negative δ^{34}S values of –19.8 and –21.7 per mil were obtained for colloform sphalerite of black color ("black schalenblende") and fine-grained euhedral sphalerite from the 1st Cardita horizon, respectively. A (nonseparable) mixture of orange and dark sphalerite plus Zn-dolomite from the Crest horizon (Kalkscholle 38) yielded δ^{34}S –21.7 per mil. Most samples from the other ore horizons also yielded less negative δ^{34}S values ranging from –22.9 to –8.3 per mil (Table 6).

Microscopic observations suggest that the less negative values are often related to microareas and samples showing increasing replacement of carbonate and sphalerite by fluorite. This is documented, for example, in sample Bl-5 from the Antoni district at Bleiberg (Table 6). Sample Bl-5 1b contains ~0.1 vol percent CaF_2 and has a δ^{34}S value of –26.3 per mil, whereas sample Bl-5 1c contains ~1 vol percent of CaF_2 and has a δ^{34}S value of –22.2 per mil. A similar trend is seen in the Rudolf district (Glantschnigg), where fluorite constitutes as much as 15 vol percent; the δ^{34}S of the sphalerite

TABLE 6. Sulfur Isotope Data of Sulfides and Anhydrite from Bleiberg Zn-Pb Deposit

Sample no., location	Description	$\delta^{34}S$ (‰)	Remark
	1st Cardita horizon		
Bl-5, 1a, Antoni	Sphalerite, composite 3 mm layer of fine-grained and microglobular ZnS ~35%, calcite ~60%, ± argillaceous material, ± fluorite	–25.7	MUL
Bl-5, 1b, Antoni	Sphalerite, brown layer composed of ZnS microglobules, minor calcite, ± argillaceous minerals, ± fluorite	–26.3	MUL (VII; Fig. 3A)
Bl-5, 1c, Antoni	Sphalerite, light brown layer composed of fine-grained ZnS, relics of ZnS microglobules, calcite, ± clays, ± fluorite	–22.2	MUL (III; Fig. 3A)
Bl-5, Antoni	Sphalerite (brown banded schalenblende) containing banded Fe-oxysulfides ~25–30%; drilled out of polished section	–30.2	MUL (IV; Fig. 3A)
Bl-5, Antoni	Sphalerite, light brown, 3-mm-zoned ZnS sphere replacing banded Fe-Pb-Zn-oxysulfide; drilled out of polished section	–30.5	MUL (5)
Bl-5, H, Antoni	Sphalerite, 3-mm-thick layer with ZnS microglobules ~80%, silicified clay matrix, ± fluorite	–28.8	MUL (I; Fig. 3A)
Bl-5, K, Antoni	Sphalerite, semi-massive brownish ZnS composed of ZnS cemented relics of microglobules	–26.5	MUL (II; Fig. 3A)
Bl-5, G, Antoni	Sphalerite, banded ZnS (reddish brown to whitish schalenblende)	–29.2	MUL (V; Fig. 3A)
Bl-5, A, Antoni	Mixture of fibrous galena and sphalerite forming colloform and spherical intergrowths plus relics of oxysulfides	–31.8	MUL (VIII; Fig. 3A)
Bl-5, C, Antoni,	Marcasite, fine-grained	–26.0	MUL (VI; Fig. 3A)
Bl-20, Antoni 6th level	Sphalerite banded with relics of ZnS microglobules	–26.4	
Antoni 6th level	Sphalerite, banded ZnS (black schalenblende)	–19.8	
Max Georgi, 2nd Lauf	Sphalerite, so-called "Röhrenerz" schalenblende, ZnS microglobules, fluorite	–27.2	
Unterfahrungsstollen	Sphalerite, fine-grained, gray layer of euhedral ZnS	–21.7	
	Crest horizon		
Kalkscholle 38	Mixture of sphalerite and Zn-dolomite, clast of orange ZnS after Zn-dolomite rimmed by dark ZnS; ~20% Zn-dolomite	–21.7	MUL (1)
Kalkscholle	Sphalerite with ZnS microglobules 35–40%; drilled out of polished section	–27.9	Collection Mosser (2)
Kalkscholle	Sphalerite replacing layer with relics of microglobules, drilled out of polished section	–28.2	Collection Mosser (3)
Bl-21 A*	Sphalerite, massive coalesced ZnS microglobules, traces of calcite	–28.9	Collection Mosser
Antoni West, 8th level			
Bl-21 B	Sphalerite, massive coalesced ZnS microglobules, ~15% calcite, ~3% fluorite	–27.8	
Bl-21 C	Sphalerite, massive coalesced ZnS microglobules, ~6% calcite	–29.3	
Bl-21 D	Sphalerite, massive coalesced ZnS microglobules, ~10% calcite, ~5% fluorite	–28.1	
Bl-21 E	Sphalerite, massive coalesced ZnS microglobules, ~8% calcite, ~2% carbonaceous material	–28.9	
Bl-21 F	Sphalerite, massive coalesced ZnS microglobules, ~6% calcite	–29.2	
Bl-21 G	Sphalerite, massive coalesced ZnS microglobules, ~10% calcite	–29.3	
Bl-21 H	Sphalerite, massive coalesced ZnS microglobules, ~15% calcite, ~1% fluorite	–28.3	
	Other ore horizons		
Rudolf (Glantschnigg)	Sphalerite layers composed of very fine-grained euhedral ZnS ~20%, calcite ~60%, fluorite ~15%, quartz ~5%, relics of microglobules	–22.9	
Maxer Bänke	Mixture of microglobules with carbonate core replaced by fluorite ~45%, sphalerite ~25%, dolomite ~20% and marcasite ~10%	–17.8	No. 43 (Fig. 4F)
Maxer Bänke	Sphalerite, dark brown euhedral ZnS crystals ~15%, yellow-brown microglobules in carbonate matrix (~40% ZnS, ~30% CaF_2), marcasite ~10%, quartz ~5%	–8.3	No. 44
Antoni 5th level	Sphalerite, euhedral crystal at the contact between blue anhydrite and coarse-grained calcite	–20.3	
Stefanie 11th level	Sphalerite, single euhedral crystal	–9.1	
	Anhydrite, blue	+20.2	
	Anhydrite, blue	+20.6	

MUL—sample from University of Leoben
*Samples Bl-21 A to H were separated from two polished sections of this sample by microcutting and drilling

that is texturally intergrown with fluorite is –22.9 per mil. Similarly, sphalerite from the Maxer Bänke horizon that is fluorite rich (~45 vol %) yielded a $\delta^{34}S$ value of –17.8 per mil (Fig. 4F). Texturally younger sphalerite that developed at the contact between blue anhydrite and coarse calcite has a value of –20.3 per mil. The least negative values (–8.3 and –9.1‰) were recorded from larger euhedral sphalerite crystals. Blue anhydrite displays positive $\delta^{34}S$ per mil values (+20.2 and +20.6‰; Table 6).

Discussion

Textural evidence for involvement of microorganisms in formation of Pb-Zn ores

In the following, we will discuss the concept that microbial processes were involved in the formation of some of the above-documented macro- to nanotextures. Microglobular sphalerites, as documented from Bleiberg in this study, have been reported from other carbonate-hosted Pb-Zn deposits

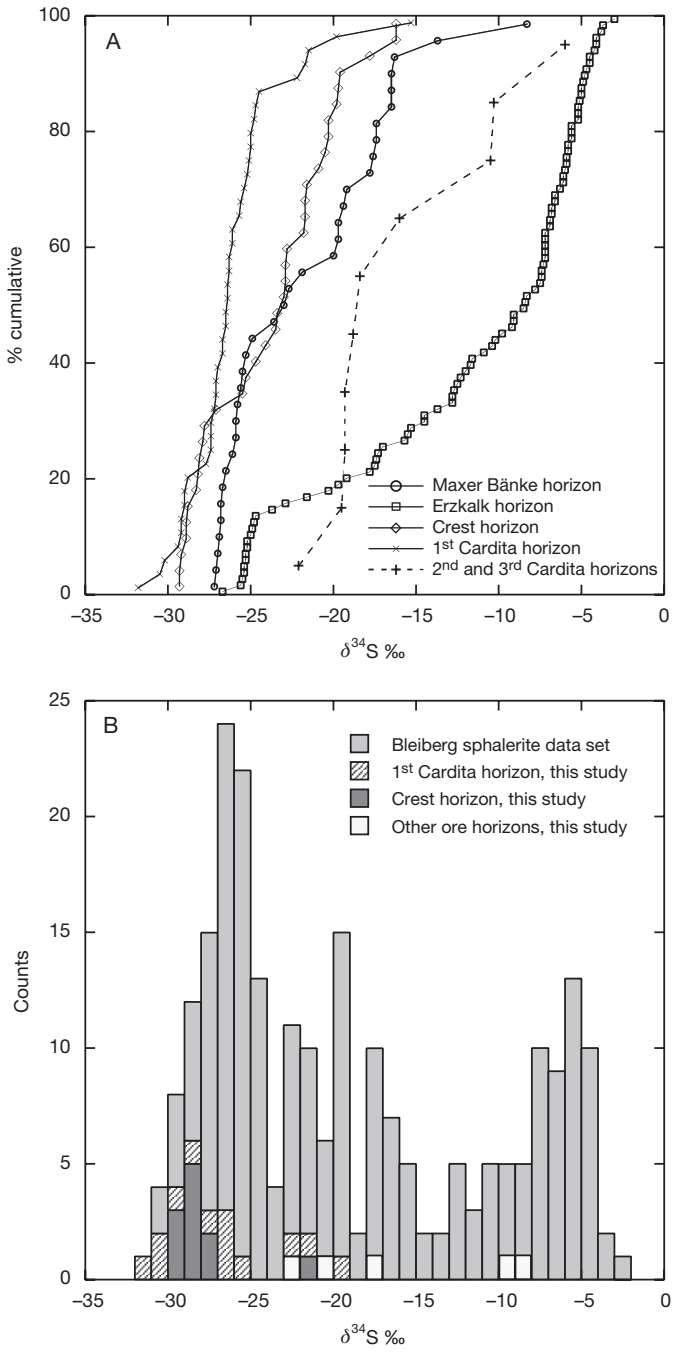

FIG. 8. Sulfur isotope data of sphalerite from the Bleiberg Pb-Zn deposit. (A) Cumulative frequency diagram of $\delta^{34}S$ values of sphalerite from different ore horizons (for details, see Schroll and Rantitsch, 2005). New analyses are included in the data set. The first Cardita, Crest and Maxer Bänke horizons are dominated by negative $\delta^{34}S$ values. Less negative values are known from the second and third Cardita horizons (only limited data available). The Erzkalk horizon is characterized by the least negative sulfur isotope values. (B) Histogram of $\delta^{34}S$ values of sphalerite comparing the new sulfur isotope data from the first Cardita, Crest and a few other ore horizons (this study) with the Bleiberg sphalerite data set compiled by Schroll and Rantitsch (2005). The data from this study are among the most negative sulfur isotope values reported from Bleiberg. By comparing A and B it becomes obvious that the population having a maximum at about –6 per mil mostly reflects the Erzkalk horizon.

before (Kucha et al., 1990, 2001, 2005) and were interpreted as mineralized peloids of biogenic origin, based on comparison of the micro- to nanotextures with those observed in sediments and recent ZnS biofilms (Labrenz et al., 2000; Druschel et al., 2002).

In this paper, we adhere to the definition of the term "peloid" as used by Chafetz (1986), who described marine peloids as, "…elliptical to spherical bodies …, generally 20–60 μm in diameter, composed of a fine-grained nucleus and a more coarsely crystalline dentate rim." The nuclei (cores) of modern marine carbonate peloids are composed of fossil bacterial clumps and are often surrounded by rims of calcite crystallites; similar peloids were recorded from hot, sulfur-rich travertine depositing sites (Chafetz, 1986). Sphalerite microglobules from Bleiberg that were least affected by diagenetic changes show similar microtexture (i.e., size and internal structure) to recent marine peloids (Chafetz, 1986) but they often have a sphalerite rim instead of a (magnesian) calcite corona (Fig. 4D, Kucha et al., 2005). In Bleiberg, the nuclei of peloids contain μm to submicrometer, elongated forms (microfilaments) and are composed of Zn-rich calcite, sphalerite, Fe smithsonite, or oxysulfides. The dentate rim is, as a rule, composed of a different material than the core, most often of sphalerite, less often of oxysulfides or pyrite (Kucha et al., 2005).

Accumulations of peloids can occur in isolated microcavities in poorly cemented sediments rich in organic material, but they are also abundant as parts of surface crusts and in microbial mats forming at the sediment-water interface (Chafetz, 1986). Some of the darker, wavy, and discontinuous domains or bands in the samples studied (Fig. 3A, B) are very rich in microglobular sphalerite (Fig. 4A, C); they are best interpreted as peloid accumulations in microbial (bacterial) mats.

One of the pertinent problems is the interpretation of the observed macro- and microtextures. Are they directly related to the activity of sulfate-reducing bacteria-precipitating sulfides, or are they merely the products of later replacement of preexisting sedimentary features in the carbonate host rocks? Hence, which mineralogical and chemical criteria can be used to examine and positively identify the direct involvement of microbes in the formation of ancient Pb-Zn ores? Recent research on natural and laboratory ZnS-precipitating bacterial films elucidates the following key criteria (Labrenz et al., 2000; Druschel et al., 2002; Labrenz and Banfield, 2004): (1) The presence of abundant, micrometer-scale spherical aggregates composed of sphalerite nanoparticles, which are expected to convert eventually into larger, micron-scale crystals of sphalerite; (2) the presence of microscale filamentous forms representing either individual sulfate-reducing bacteria or their extracellular polymeric substance set within agglomerations of micrometer-scale spherical aggregates, which themselves are composed of nanoglobular particles; (3) strongly negative sulfur isotope signature related directly to biochemical reduction of oxidized sulfur species (e.g., seawater SO_4^{2-}).

Our observations during very high magnification (FESEM imaging) on etched peloid cores support the concept of direct microbial sphalerite precipitation. Micro- to nanotextures include filamentous forms from submicron to 2 μm, accompanied by numerous spherical sphalerite bodies ranging from 30 to 50 nm. Kucha et al. (2005) have already interpreted these

sphalerite microfilaments and nanospheres as relics of sulfate-reducing bacteria. This interpretation was mostly based on morphological criteria because strikingly similar micro- to nanotextures were documented in natural biofilms composed of sphalerite and formed by BSR in the flooded Piquette Pb-Zn deposit, Tennyson, Wisconsin (Labrenz et al., 2000; Labrenz and Banfield, 2004).

Very similar morphological characteristics have been recorded from ephemeral hypersaline lakes in a near-surface, evaporitic lagoonal environment where dolomite nanospheres forming larger microglobules composed of dolomite are precipitated by sulfate reducing bacteria (Wright and Wacey, 2005). Several other recent studies (in the laboratory and on natural samples) also confirmed that dolomite nanospheres precipitate on the cell surface or on extracellular polymeric substances and subsequently aggregate to larger globules (Wright and Wacey, 2005; Aloisi et al., 2006; Bontognali et al., 2008; Sánchez-Román et al., 2008).

In this study we noted that submicron-scale spherical aggregates forming larger sphalerite microglobules (Fig. 5B, C) are preserved in some samples; in places, sphalerite nanoparticles are not yet fully aggregated (e.g., center of Fig. 5D). It must be noted that these ubiquitous sphalerite nanospheres are too small to be fossil (nano) bacteria (Southam and Donald, 1999; Ehrlich and Newman, 2009). Instead, we interpret the nanospheres as in situ products of bacterial metabolism. The sphalerite nanospheres are always closely associated with mineralized microfilaments (Fig. 5B, C); the latter are interpreted to be either mineralized relics of former bacteria with tubular morphology or mineralized microbial extracellular polymeric substance. Nucleation of nanospheres within extracellular polymeric substance is a strategy used by some carbonate-producing BSR to prevent rapid cell entombment (Bontognali et al., 2008). We envisage that the same mechanism was adapted by sulfide-precipitating species. Zinc, transported by hydrothermal fluids to the habitat where these microorganisms lived, was used to fix the toxic, reduced sulfur species (e.g., H_2S) liberated during biogenic sulfate reduction. Availability of zinc might therefore even have promoted abundant growth of microbial communities. In summary, we think that microorganisms were directly involved in the formation of sphalerite ores at Bleiberg Pb-Zn deposit.

Formation mechanisms of sphalerite globules and pyrite framboids

The observed microtextures referred to in this paper as microglobular sphalerite (Fig. 4A-F) and interpreted as peloids, are the earliest forms of sphalerite in the Pb-Zn ores from Bleiberg. They are composed of sphalerite nanospheres and microfilaments (Fig. 4A-D), usually cemented with Zn-rich calcite or Zn-rich dolomite. As documented in this study, peloids are converted into sphalerite microglobules by progressive replacement of the Zn-rich calcite core by sphalerite with simultaneous increase of their size to 100 to 180 μm from the original peloid size of about 60 to 90 μm (Fig. 4A, C-E). The suggested transformation is as follows:

Peloids (Zn-rich calcite core + ZnS rim) → replacement by ZnS → ZnS microglobules.

There are, however, microglobules lacking filamentous forms. In this case it is possible that the larger sphalerite microglobules formed by nonbiogenic coalescence of nanosized sphalerite spheres, which themselves formed as metabolic products of microbial activity (see discussion above). Such small nanostructures have a very high surface energy and unbalanced surface charges (Zhang and Banfield, 1998), which are therefore sufficiently strong to cause coalescence of nanoparticles to form larger microglobules of sphalerite with a final size of 100 to 180 μm. In this case the suggested transformation path is this:

Biogenically precipitated ZnS nanospheres → coalescence driven by unpaired surface electric charges → ZnS microglobules.

Such growth via oriented aggregation of small particles (self assembly) is an alternative process to dissolution of small particles followed by atom-by-atom growth of bigger ones, and is driven by thermodynamic minimization of surface energy (Banfield et al., 2000). Formation of angular, euhedral to subhedral sphalerite crystals with sizes from 1 to 25 μm (Fig. 4D), entrapped within the calcite matrix, probably started with oriented aggregation of sphalerite nanoparticles. Progressive diagenetic recrystallization of sphalerite microglobules resulted in further grain coarsening and in the angular morphology of sphalerite crystals (Fig. 4E).

Spherical forms with morphology and size very similar to microglobular sphalerite are also documented for framboidal pyrite. Pyrite framboids are composed of clumps of Zn-rich FeS_2 nanospheres (Fig. 6A, B; Table 3). It is suggested that framboidal pyrite crystals formed by aggregation of microspherical precursor forms, which are composed of nanoglobular FeS_2. The process of growth via oriented aggregation is supported by mineral chemical data. The stoichiometry of the precursor sulfide is close to FeS_2, but has much higher Zn content than framboidal pyrite (Table 3). This is in accordance with refinement of the host pyrite lattice from incompatible Zn during recrystallization.

Interpretation of sulfur isotope data

Sulfur isotope data from Bleiberg were compiled by Schroll et al. (1983) and more recently by Schroll and Rantitsch (2005). Sulfur isotope data of sphalerites from this data set (n = 354) are shown together with our new isotope data in Figure 8. Statistical treatment of this data set allowed distinguishing three populations (Schroll and Rantitsch, 2005). The first population has a well-defined peak at about –6 per mil $\delta^{34}S$. This population is dominant in the Erzkalk horizon (Fig. 8A) and has been interpreted as sulfur from an epigenetic-hydrothermal fluid source (Schroll and Rantitsch, 2005). A second population has a broad peak between –20 and –13 per mil $\delta^{34}S$. This population may be due to mixing of hydrothermal and bacteriogenic sulfur of the third population. Population 3 has a well-defined peak between –29 and –25 per mil $\delta^{34}S$. This population is dominant in the Cardita and Crest horizons but is, to some extent, also present in the other ore horizons (Fig. 8A). It has been ascribed to bacteriogenic reduction of seawater sulfate (BSR). The mean $\delta^{34}S$ value of barite is ~15 per mil, and values of anhydrite range between +15 and +20 per mil. In comparison, the global composition

of the seawater sulfate in the Carnian is +15.8 ± 0.4 per mil (Holser, 1977).

Microareas of the samples studied with the best-preserved biogenic microtextures (microbial mats, peloid-rich bands) have $\delta^{34}S$ values of about –28 to –29 per mil. These new data are at the lower end of population 3 of bacteriogenic origin (Fig. 8B). The isotopic composition of these sphalerites is ~44 to 45 per mil lighter than the Carnian seawater sulfate. Similar Δ values are often recorded from sulfides and coexisting sulfates in nature and the standard interpretation, known as the Rees model, provides a maximum Δ value of –46 per mil for the sulfur isotope fractionation (Rees, 1973). The clear mode of population 3 supports bacterial sulfate reduction in an open system (Seal, 2006).

The heavier values (up to –20.8‰) recorded in several samples are more difficult to explain. They seem to correspond to microareas and samples where fluorite is a more common gangue mineral. Fluorite is replacing peloid calcite cores, microglobular sphalerite, and oxysulfides and is therefore interpreted to postdate the stage of biogenic sphalerite mineralization (Fig. 4F). The heavier values could reflect (1) physical mixing of sulfides having a light bacteriogenic sulfur isotope signature (population 3) with sulfides having isotopic heavier sulfur (population 1; e.g., sphalerite formed together with later F-bearing hydrothermal fluids), or (2) change from an initially open to a restricted (or even closed) sulfur isotope system during ongoing sulfate reduction. With respect to (1), it must be remembered that the material analyzed was drilled out from polished sections and slabs. Although the drilling areas were carefully selected, any material change with drilling depth was difficult to control. Only true in situ analyses (e.g., SIMS) could overcome this limitation. Because the discussed values (~–20‰) are still significantly lighter than the hydrothermal signal (~–6‰), any physical admixture of heavier sulfur would, however, be minor. With respect to (2), it can be hypothesized that the sulfur reservoir evolved over time from an open to a closed system (reservoir). In the initial stage with unlimited access and exchange of seawater with the pore water in the uppermost anoxic zone below the sediment-seawater interface, the system can be regarded as open; i.e., the available sulfur reservoir (seawater) is unlimited. During diagenesis due to compaction, cementation processes, etc., exchange of pore fluids with seawater becomes more and more restricted and the system evolves to partly or even totally closed conditions. Depending on the diffusion to reduction rate, this would result in broad, skewed frequency distributions in the histograms and shift of the (broadened) peak to less negative $\delta^{34}S$ values (for detailed explanations, see Seal, 2006).

Another possible factor influencing sulfur isotope composition of sulfides formed by BSR is the microbial community. Not all taxonomic groups of sulfate-reducing prokaryotes fractionate sulfur with the same efficiency and there is a wide variation in isotopic composition produced by microorganisms (~2–42‰; Detmers et al., 2001). In marine settings, the fractionation associated with BSR ranges from 15 to 71 per mil, and this extreme variation found in nature is likely due to reoxidation of sulfides and effects associated with disproportionation of intermediate sulfur species (Seal, 2006). This mechanism, also known as "reversible multistep sulfite-sulfide reaction" going through trithionate and thiosulfate, (Cypionka, 1995; Brunner and Bernasconi, 2005) may have some direct merits for the Bleiberg case. Sulfite (Kucha and Stumpfl, 1992), trithionate, and thiosulfate are confirmed in the samples studied (Tables 4, 5). Moreover, oscillatory, reversible (?) zoning of sulfur valences has been observed in oxysulfides forming a kind of microbial mat within banded sphalerite (Kucha and Stumpfl, 1992). A similar case has been described from Engis, Belgium (Kucha, 1989). This calls for urgent and detailed study of oxysulfide compounds, which may be a useful and handy tracer of bacteriogenic processes in the deposits in question.

Compounds of mixed sulfur valence (oxysulfides) have also been documented in the studied samples. Relicts of oxysulfides are preserved in banded sphalerite that is interpreted as a microbial mat in sample Bl-5 from Antoni (see microarea IV; Figs. 3A, 4B). These samples yielded the most negative sulfur isotope values of all sphalerites (–30.5, –30.2‰) in the new data set. Fibrous galena, which is also associated with oxysulfides, is ~3 per mil lighter than the coexisting bacteriogenic sphalerite (microarea VIII, sample Bl-5A; Table 6). Therefore, oxysulfides may have been instrumental in causing the additional negative shift in the $\delta^{34}S$ values. The mechanism suggested involves thiosulfate $(Fe,Zn,Pb)S_2O_3$ (or similar intermediate sulfur species like trithionate; Table 4) during recrystallization of sphalerite. As evident in Table 5, these compounds have different sulfur valences. In thiosulfate, the outer S atom has a valence of –1 and the inner one has a valence of +5. The S^{1-} and S^{5+} atoms are connected by S-S bonds. During recrystallization or reaction of these phases, the S-S bonds containing isotopically lighter S atoms are more easily broken and the liberated lighter sulfur will be preferentially incorporated in newly formed fibrous sphalerite or fibrous galena. The heavier sulfur atoms may be fixed in anhydrite inside small vugs or in microfractures, as seen in the Crest ore sample (Fig. 3B).

There is some debate in the literature about the processes providing isotopically light sulfur that is reported from some carbonate-hosted Pb-Zn deposits (e.g., Bleiberg, Navan; Schroll et al., 1983; Fallick et al., 2001; Schroll and Rantitsch, 2005). The two competing (but not excluding) models are abiotic thermochemical sulfate reduction (TSR) versus biogenic bacteriogenic sulfate reduction. Abiotic sulfur reduction is the controlling process for the temperature range >120°C, in which sulfate-reducing microorganisms cannot survive (Ehrlich and Newman, 2009). Gradual sulfate reduction through mixed sulfur valence oxyanions (e.g., thiosulfate) can produce, by molecular exchange, a bacteria-type sulfur isotope signature (Ohmoto and Lasaga, 1982). Both bacteriogenic as well as thermochemical reduction of marine sulfate was proposed to explain the wide variation (+2 to –29‰) in sulfur isotope composition of sulfides from Pb-Zn deposits in the eastern Drau Range, although bacteriogenic sulfate reduction was the preferred model to explain the very light isotope population (Kuhlemann et al., 2001; Schroll and Rantitsch, 2005).

Most of the new sulfur isotope data correspond to population 3, with a well-defined maximum at –26 to –28 per mil (Fig. 8B). Note that this population corresponds to orebodies of major economic importance at Bleiberg (e.g., Cardita and Crest horizon, Cerny, 1989a), and is mostly lacking in the

eastern Drau Range (e.g., Mezica; Kuhlemann et al., 2001). Hence, there exist regional differences. The bacteriogenic signature is very characteristic for some, but not all, ore horizons at Bleiberg. Similar to some Irish Pb-Zn deposits, bacteriogenic sulfate reduction is regarded as a key process in formation of the Bleiberg Pb-Zn deposits; Fallick et al. (2001) calculated that in Ireland, ≥90 percent of the sulfur necessary to form the giant Navan deposit was derived by bacteriogenic sulfate reduction of seawater sulfate.

Factors constraining biological processes

Despite diagenetic recrystallization, microbial mats, peloids, filamentous forms, and biogenically formed sphalerite nanospheres are locally very well preserved and ubiquitous in some Zn-Pb ores at Bleiberg (first Cardita horizon, Crest horizon). In some studied samples, microbial mats (recurrent sphalerite layers up to several cm thick entirely composed of peloids or their phantoms) and even massive layers of banded sphalerite reveal, after etching, about 30 vol percent of microglobular sphalerite. As outlined above, recent biofilms containing nm- to μm-sized spherical ZnS precipitates, and microfilaments (Labrenz et al., 2000; Druschel et al., 2002; Labrenz and Banfield, 2004) are strikingly similar to fossilized textures observed at Bleiberg.

Similar bacterial mats were recorded from recent hydrothermal vents forming on polymetallic sulfide surfaces and composed of both unicellular and filamentous bacteria (Wirsen et al., 1993). Molds resembling dissolved bacteria were also observed in multilaminated sulfide walls of vestimentiferan tube worms in Silurian hydrothermal vents (Little et al., 1997). Peloids, interpreted as fossilized bacteria, were reported from mineralized karst and stromatactis cavities, paleoweathering crusts, and breccia ores in strata-bound carbonate-hosted Zn-Pb deposits in Belgium, Ireland, and Poland (Kucha, 1988; Kucha et al., 1990).

Microorganisms can live in habitats of varying depth; e.g., in the hydrosphere, on the sea floor, in the underlying unconsolidated sediment close to the seawater sediment interface, as well as in the pore space and open cavities down to considerable depths (Ehrlich and Newman, 2009). Microbes are found several kilometers below the Earth's surface and microbial alteration of basalt and marine sediments was found to occur many hundred meters below the sea floor (Banfield and Welch, 2000). Subsurface aquifers (including deep aquifers in igneous rocks) have a high microbe density, with numbers ranging from 10^5 to 10^8 cells per cm^3. Microbe densities in slimes and biofilms are about 10^{12} cells per cm^3 (Banfield and Welch, 2000). It is therefore possible that subsurface environments can support a higher density of microbes in the pore network realm, provided that temperature stays below ~120°C. Temperature is one of the key factors limiting direct involvement of BSR in biogenic sulfide precipitation. Most microorganisms are sensitive to changes in temperature and their optimum living conditions are well below 100°C, although some thermophiles are known to be active up to 120°C (Ehrlich and Newman, 2009).

Supply and reactivity of organic matter is another limiting factor for BSR in normal (oxygenated) marine settings (Seal, 2006). It has been calculated by Rickard (1973) that to deposit more than 1 percent of metal by bacteria, an enriched source of metal (hydrothermal fluid) and a minimum of 0.1 percent of carbon are required. It appears, however, that sulfate-reducing bacteria can use hydrogen (Nedwell and Banat, 1981; Detmers et al., 2001) or CH_4 (Ehrlich and Newman, 2009) for sulfate reduction. This would significantly lower the organic carbon requirement in the host rock, which in the Bleiberg massive sulfide ore varies between 0.05 and 0.69 wt percent. Schneider (1964) pointed out the presence of organic carbon in the host rocks of Alpine Pb-Zn deposits and he argued that this is one of the factors controlling Pb-Zn mineralization in the Eastern Alps. However, quantitative data about the organic carbon contents of the host rocks distal to the orebodies at Bleiberg are not available.

Genetic models for Alpine Pb-Zn deposits

In the last 60 years, two contrasting genetic models have mainly been discussed for Alpine carbonate-hosted Pb-Zn deposits. Syngenetic-syndiagenetic models postulating contemporaneous formation of the ore and host rocks in the Middle Triassic (e.g., Maucher and Schneider, 1967; Schulz, 1968; Cerny, 1989b; Schroll, 1997, 2006) contrast with Mississippi Valley-type (MVT) models, the latter arguing for Pb-Zn mineralization in the Upper Triassic to Early Tertiary related to late diagenetic burial (e.g., Jicha, 1951; Bechstaedt and Dohler-Hirner, 1983; Zeeh and Bechstaedt, 1994; Zeeh et al., 1999; Kuhlemann et al., 2001; Leach et al., 2003).

Mineralization styles at Bleiberg vary widely (see summary in Schroll, 2008), ranging from stratiform–strata-bound ores (Erzkalk, Cardita, Max horizons) in the upper part of the Wetterstein Formation, either interpreted as synsedimentary ores (Schulz, 1968) or later fillings ("internal sediments") of karst cavities (Siegl, 1957; Bechstaedt, 1975a; Zeeh and Bechstaedt, 1994), through various types of breccia and metasomatic replacement ores, to discordant veins (e.g., Schulz, 1966; Schulz, 1985).

Larger (tens of meters thick) bodies of sedimentary breccias ("Resedimentbreccie") were documented from the first and third Cardita horizons, and the uppermost ~150 m of the Wetterstein Formation (Schulz, 1975, 1985). These dolomite-dominated breccias are stratigraphically equivalent to the limestone-hosted strata-bound ores (Erzkalk horizon) of the Wetterstein Formation and were seen as evidence for synsedimentary tectonics (Schulz, 1975). Tectonic breccias are especially important in the western parts of the former Bleiberg mine in the Crest horizon, where they hosted high-grade Zn-rich ores (Schulz, 1973; Cerny, 1989b). Thinner layers of dark, fine-grained breccias associated with dolomitized stromatolites (algal mats) and green marls are the product of cyclic and rhythmic sedimentation in the lagoonal facies and reflect the cyclic changes from subtidal to intersupertidal conditions. Sea level changes and synsedimentary tectonics resulted in temporary emersion of the host sediments above the sea level and formation of karst cavities and this type of breccia (Bechstaedt, 1975b; Brigo et al., 1977). These breccias are of special importance for the Erzkalk horizon.

Fluid inclusions were used to constrain the formation temperatures of Pb-Zn deposits in the Drau Range. Leach et al. (2003) briefly summarized the scarce existing fluid inclusion data. It must be noted that fluid inclusion data are only available from late diagenetic carbonate cements, fluorite, and,

very rarely, sphalerite (Zeeh et al., 1999). The fluids are aqueous, with low to moderate salinity. Inclusions in fluorite from the first main stage of ore formation (according to the classification of ore stages proposed by Leach et al., 2003) yielded temperatures of homogenization (Th) of 170° to 190°C and total salinities of 18 to 21 wt percent NaCl equiv. Fluorite from the second main ore stage yielded lower homogenization temperatures (T_h 120°–140°C) and slightly higher total salinities (22–25 wt % NaCl equiv). An even younger fluorite generation yielded lower homogenization temperatures and lower salinities (T_h 76°–120°C; 6–10 wt % NaCl equiv). Saddle dolomite from the Wetterstein Formation and Raibl Group that pre- and postdates mineralization yielded similarly low homogenization temperatures (T_h 77°–109°C) but higher salinities (15–19 wt % NaCl equiv; Leach et al., 2003). No fluid inclusion data for sphalerite are available from Bleiberg. Data from only one single sphalerite sample from the Jauken deposit were reported (T_h 92°–129°C, 8–12 wt % NaCl equiv); however, details about its petrography are lacking (Zeeh et al., 1999; Leach et al., 2003).

Fluid inclusion data for primary fluid inclusions in two fluorite samples at Radnig (20 km west of Bleiberg; Fig. 1) yielded T_h values ranging from 76° to 117°C, and final ice melting temperatures between –5.5° and –9.0°C. From this deposit it is petrographically documented that this fluorite replaces coarse-grained saddle dolomite (Zeeh et al., 1995), one of the late diagenetic cement types, according to the cement stratigraphy established by these authors.

Two other fluorite samples from the Wetterstein Formation in the Drau Range gave slightly different results (Zeeh et al., 1995); the first sample yielded T_h 120° to 142°C, and T_m –24° to –20.4°C, whereas the second one yielded T_h 84° to 120°C, and T_m –6.3° to –3.8°C. Recalculation of densities and isochores gave minimum trapping temperatures of these fluids between 120° and 140°C (assuming hydrostatic pressure conditions of 35 MPa) and maximum trapping temperatures of 160° to 180°C (assuming lithostatic pressure conditions of 125 MPa) (for details, see Rantitsch, 2003). Some of the previous data giving very high trapping temperatures (>240°C) are much higher than the maximum temperatures obtained from basin modeling and, according to Rantitsch (2003), might even be erroneous. The thermal history of the Carnian carbonate sequences in the Drau Range at Bleiberg reached maximum temperatures of ~130°C during late diagenetic burial in the late Cretaceous-Early Tertiary (Fig. 9; Rantitsch, 2001, 2003).

It can be argued that most of these (minimum) trapping temperatures are too high for microorganisms and therefore contradict our genetic model of microbial sphalerite formation. The following arguments can be brought forward against this:

1. Entrapment of fluid inclusions in fluorite and carbonate cements was not necessarily cogenetic with biogenic sphalerite. For example, there are several stages of fluorite known from Bleiberg (see summary in Schroll, 2008), an observation which is also supported by the limited fluid inclusion data available (see summary above). Previous studies (Zeeh and Bechstaedt, 1994) already documented that fluorite and saddle dolomite postdate formation of colloform

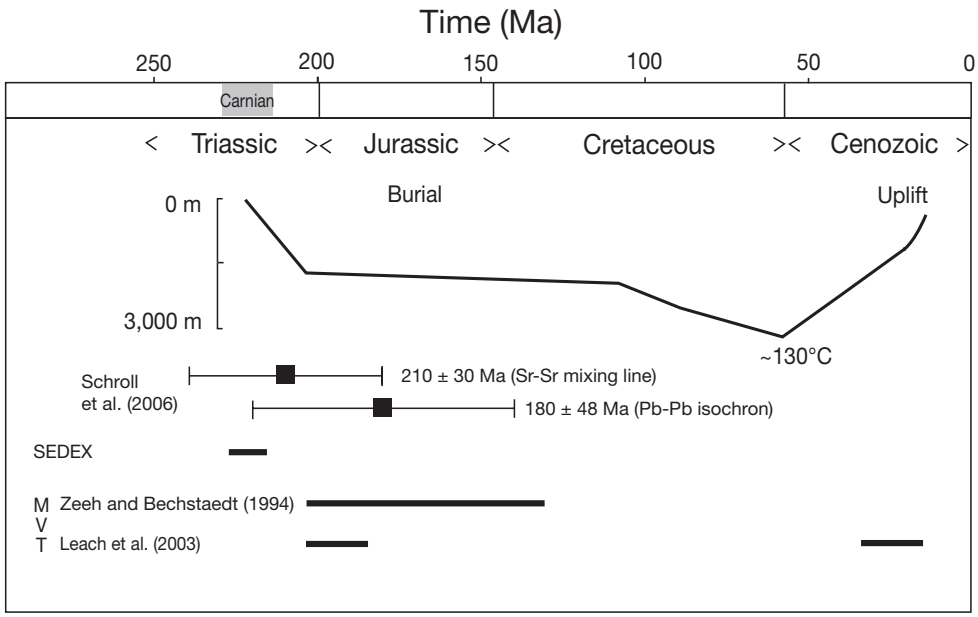

FIG. 9. Time chart summarizing the thermal and burial history of the Drau Range (simplified from Rantitsch, 2003) and models on the genesis and timing of Pb-Zn ore formation at Bleiberg. The stratigraphic age of the sedimentary rocks hosting the Bleiberg Pb-Zn deposit is Carnian. The solid line shows the burial history of the strata at the Carnian Wetterstein Formation-Raibl Group boundary, which were buried to ~3 km and heated up to ~130°C in the Late Cretaceous-early Tertiary (~50 Ma). The 210 ± 30 Ma age is the age of a mixing line recalculated from $^{87}Sr/^{86}Sr$ ratios of carbonate rocks from the Crest horizon. The uncertainty is at a minimum value of ±30 m.y. for an age of 210 Ma (for details see Schroll et al., 2006). The 180 ± 48 Ma age is a Pb-Pb isochron age of 20 ore lead samples from Bleiberg (Schroll et al., 2006). The thicker horizontal bars indicate the preferred timing of Pb-Zn mineralization according to the SEDEX versus MVT models (Zeeh and Bechstaedt, 1994; Leach et al., 2003).

sphalerite. Our own textural observations also indicate that very early formed fine-grained fluorite is replacing sphalerite with microbial microtextures (Fig. 4F). Hence, even formation of "early" fluorite postdates formation of microbially precipitated sphalerite.

2. Fluid inclusion data are only reported for a single sphalerite sample (see above) for which, however, no petrographic details are given (Leach et al., 2003). According to Zeeh et al. (1999), the studied sphalerite shows brown luminescence, which is distinct from the earlier first, "small" (fine-grained) sphalerite generation. The sphalerite containing measurable fluid inclusions could have formed, therefore, at a later diagenetic stage during burial, when sphalerite recrystallized and was remobilized.

3. Microthermometry is limited by the grain size of the host mineral because this limits the size of the fluid inclusions. In practice, it is difficult or even impossible to analyze fluid inclusions, which are much less than ~5 to 10 μm in size. Hence, the composite microglobular sphalerites that we studied are too small to host fluid inclusions of measurable size. No fluid inclusion data are therefore available for the very fine grained sphalerite ores, which are the focus of this study. All available data are from coarser-grained host minerals (late diagenetic carbonate cements, fluorite, and late-stage sphalerite) that in our opinion formed during subsequent diagenetic processes (Zeeh and Bechstaedt, 1994; Zeeh, 1995).

The possible source rocks of Pb and Zn were constrained using Pb isotopes (Koeppel and Schroll, 1988). The similarity of feldspar-lead from the crystalline basement and the ore lead indicates that the lead was mainly derived from the basement underlying the Mesozoic carbonate rocks (Paleozoic metasediments; Permoscythian sandstones). Trace elements such as Ge and Ga in sphalerite also indicate interaction of hydrothermal fluids with aluminosilicates (Schroll, 2006). From the Ga-Ge ratios, Moeller (1987) deduced leaching of these metals, together with Pb and Zn, from crustal source rocks at temperatures of ~100°C.

Proponents of the MVT model correlate formation of all Pb-Zn ore types and orebodies with the late diagenetic burial of the Drau Range carbonate platform. Zeeh and Bechstaedt (1994) suggested formation of Pb-Zn mineralization between the Late Triassic and Early Cretaceous, whereas Zeeh et al. (1995) and Leach et al. (2003) argued for a Late Triassic to Early Jurassic age and some minor ore formation later in the mid-Tertiary (Fig. 9). Rb-Sr dating of hydrothermally affected carbonate host rocks and Pb-Pb dating of galena yielded model ages of 210 ± 30 Ma (Rb-Sr dating of hydrothermally affected carbonate host rocks) and 180 ± 40 Ma (Pb-Pb dating of galena), respectively (Schroll et al., 2006, Fig. 9). These ages are not precise enough to decide in favor of MVT vs. SEDEX-type models discussed for Bleiberg, although they exclude ore formation during the deep burial; maximum burial of the Carnian Wetterstein Formation to ~3 km was not before the Late Cretaceous-Early Tertiary (Rantitsch, 2001).

In defending the MVT model for the Alpine Pb-Zn deposits, Leach et al. (2003) argued against textural and isotopic evidence provided by Kucha et al. (2001), who favor a Triassic age of Pb-Zn mineralization. Leach et al. (2003, p. 205) state, "No proof is given, however, either that the bacterial reduction is synsedimentary/early diagenetic, or that Zn-compounds are not replacive after carbonate peloids, and that the sulfide sulfur originated solely from sulfate reduction shortly after deposition, concurrent with sulfide emplacement."

We agree that one process of sphalerite peloid formation is via replacement of carbonate nuclei of the peloids. However, the carbonate cores of peloids or incompletely replaced carbonate relics contained in sphalerite are composed of Zn-rich calcite or Zn-rich dolomite. Thus, we suggest that Zn was already available during peloid formation and that Zn was transported into the unconsolidated sediment by hydrothermal fluids when the microbial peloid nuclei formed.

The isotope values of sulfides preserving bacteriogenic ore textures are among the most negative values reported from Bleiberg and Alpine-type Pb-Zn deposits. BSR was therefore the dominant process providing H_2S for formation of sulfides in the Crest and Cardita ores. Leach et al. (2003) did not exclude a bacteriogenic sulfur source, although they argued for storage of the reduced sulfur in the pore fluid for a longer time interval. Based on textural observations (microbially precipitated sphalerite nanospheres and microfilaments) our interpretation is that the reduced sulfur species liberated during microbial metabolism were fixed by reaction with Zn in situ in the habitat of these microorganisms. A high population density of microorganisms characterized this habitat (e.g., microbial mats in a hypersaline lagoon, subsurface pore space). Moreover, subsequent nonbiogenic aggregation of sphalerite nanoglobules to larger microglobular sphalerite structures occurred in relatively unconsolidated sediment during early diagenesis. It is difficult to imagine that these mineralization processes operated in deeply buried and lithified carbonate rocks as would have been necessary according to the MVT model. Although some sulfur-based thermophiles can live in higher temperature (up to 120°C) environments (e.g., submarine hydrothermal vents, Ehrlich; 1990), BSR is most efficient below this temperature. If our interpretation—that the sphalerite nanoglobules and microfilaments are the direct products of microbial metabolism—is correct, the fine-grained, Zn-rich ores from the first Cardita and Crest horizons cannot have formed at the high temperatures deduced from fluid inclusions (see above) and interpreted by MVT proponents as formation temperatures of the main ore stage (Zeeh et al., 1995; Kuhlemann et al., 2001; Leach et al., 2003).

At present, we cannot exclude that some Pb-Zn ores at Bleiberg (e.g., those in the Erzkalk horizon), in which microbial ore textures have not yet been recognized and which show a heavier sulfur isotope signature, formed through nonbiogenic processes. Abiotic TSR may have been important during formation of these nonbiogenic ores. Pressure-T-X conditions reported from fluid inclusions and specific "late" cement types might correspond with this subsequent mineralization that occurred during diagenetic burial.

Conclusions

Pb-Zn ores from Bleiberg, the largest carbonate-hosted Pb-Zn deposit in the Alps, frequently contain nano- to macrotextures of biogenic origin, which were made visible by etching and optical FESEM. The interpretation of these textures is

largely through comparison with modern environments where biogenic processes are active. Microscale globular sphalerite is abundant in rhythmically banded and chaotic breccia ores in the Crest and Cardita horizons where it is concentrated in what is interpreted as microbial mats. These sphalerite microglobules can form by two different processes, either by replacement of peloids of biogenic origin or by nonbiogenic aggregation of sphalerite nanoglobules. The latter are associated with mineralized microfilaments interpreted as bacteria or mineralized, extracellular, polymeric substances. The observed nanofeatures are strikingly similar to those produced by sulfate-reducing bacteria precipitating sphalerite nanospheres in recent natural biofilms and in cell cultures. Based on this analogy, we propose that sulfate-reducing bacteria precipitated the sphalerite nanoglobules in situ as metabolic by-products during an early stage of ore formation. Sulfur isotope data support the biogenic origin of these ores and bacteriogenic sulfate reduction is regarded as the key process for providing isotopic light sulfur typical for the studied Crest and Cardita ores. Microbial in situ fixation of Zn must have operated at lower temperatures (<120°C), preferably during the sedimentation or early diagenetic stage. This interpretation is inconsistent with the MVT model that postulates formation of Alpine Pb-Zn deposits during late diagenetic burial in the Late Triassic-Early Jurassic. Sulfur isotope analyses should be coupled with the study of textures down to the nanoscale to evaluate the contribution of biogenic versus nonbiogenic processes in formation of carbonate-hosted Pb-Zn deposits.

Acknowledgments

Thanks are due to H. Mühlhans for help with sample preparation and electron microprobe analyses. We thank G. Rantitsch for fruitful scientific discussions and his prereview comments on the paper. Reviews by S. Golding, an anonymous reviewer, and the careful editorial input by editor K. Kelley helped to improve this manuscript. Financial support of the Austrian Academy of Sciences (ÖAW), Commission for Mineral Raw Materials, is gratefully acknowledged.

REFERENCES

Aloisi, G., Gloter, A., Kruger, M., Wallmann, K., Guyot, F., and Zuddas, P., 2006, Nucleation of calcium carbonate on bacterial nanoglobules: Geology, v. 34, p. 1017–1020.

Banfield, J.F., and Welch, S.A., 2000, Microbial controls on the mineralogy of the environment, *in* Vaughan, D., and Wogelius, R.A., eds., Environmental mineralogy: 2: European Mineralogical Union Notes in Mineralogy: Budapest, Eötvös University Press, p. 173–196.

Banfield, J.F., Welch, S.A., Zhang, H., Ebert, T.T., and Penn, R.L., 2000, Aggregation-based crystal growth and microstructure development in natural iron oxyhydroxide biomineralization products: Science, v. 289, p. 751–754.

Bawden, T.M., Einaudi, M. T., Bostick, B.C., Meibom, A., Wooden, J., Norby, J.W., Orobona, M.J.T., and Chamberlain, C.P., 2003, Extreme ^{34}S depletions in ZnS at the Mike gold deposit, Carlin Trend, Nevada: Evidence for bacteriogenic supergene sphalerite: Geology, v. 31, p. 913–916.

Bechstaedt, T., 1975a, Lead-zinc ores dependent on cyclic sedimentation (Wetterstein limestone of Bleiberg-Kreuth, Carinthia, Austria): Mineralium Deposita, v. 10, p. 234–248.

——1975b, Sedimentologie und Diagenese des Wettersteinkalkes von Bleiberg-Kreuth: Berg- und Huettenmännische Monatshefte, v. 120, p. 466–471.

Bechstaedt, T., and Dohler-Hirner, B., 1983, Lead-zinc deposits of Bleiberg-Kreuth: AAPG Memoir, v. 33, p. 55–63.

Bontognali, T.R.R., Vasconcelos, C., Warthmann, R.J., Dupraz, C., Bernasconi, S.M., and McKenzie, J.A., 2008, Microbes produce nanobacteria-like structures, avoiding cell entombment: Geology, v. 36, p. 663–666.

Brigo, L., Kostelka, L., Omenetto, P., Schneider, H.J., Schroll, E., Schulz, O., and Strucl, I., 1977, Comparative reflections on four Alpine Pb-Zn deposits, *in* Klemm, D.D., and Schneider, H.J., eds.: Time- and stratabound ore deposits: Berlin-Heidelberg-New York, Springer-Verlag, p. 273–293.

Brunner, B.B., and Bernasconi, S.M., 2005, A revised isotope fractionation model for dissimilatory sulfate reduction in sulfate reducing bacteria: Geochimica et Cosmochimica Acta, v. 69, p. 4759–4771.

Cerny, I., 1989a, Current prospecting strategy for carbonate-hosted Pb-Zn mineralizations at Bleiberg-Kreuth (Austria): Economic Geology, v. 84, p. 1430–1435.

——1989b, Die karbonatgebundenen Blei-Zink-Lagerstaetten des alpinen und ausser-alpinen Mesozoikums: Die Bedeutung ihrer Geologie, Stratigraphie und Faziesgebundenheit für Prospektion und Bewertung: Archiv für Lagerstättenforschung der Geologischen Bundesanstalt, v. 11, p. 5–125.

Chafetz, H.S., 1986, Marine peloids; a product of bacterially induced precipitation of calcite: Journal of Sedimentary Petrology, v. 56, p. 812–817.

Cypionka, H., 1995, Solute transport and cell energetics: Biotechnology Handbooks 8, Plenum Press, p. 151–184.

Detmers, J., Bruecher, V., Habicht, K., and Kuever, J., 2001, Diversity of sulfur isotope fractionations by sulfate-reducing prokaryotes: Applied and Environmental Microbiology, v. 67, p. 888–894.

Druschel, G.K., Labrenz, M., Thomsen-Ebert, T., Fowle, D.A., and Banfield, J.F., 2002, Geochemical modeling of ZnS in biofilms: An example of ore depositional processes: Economic Geology, v. 97, p. 1319–1329.

Ehrlich, H.L., 1990, Microbial mineral recovery: New York, McGraw-Hill, 454 p.

Ehrlich, H.L., and Newman, D.K., 2009, Geomicrobiology: 5th ed.: Boca Raton, Florida, CRC Press, 628 p.

Evans, A.M., 1993, Ore geology and industrial minerals: An introduction: Oxford, Blackwell Scientific Publications, 390 p.

Fallick, A.E., Ashton, J.H., Boyce, A.J., Ellam, R.M., and Russell, M.J., 2001, Bacteria were responsible for the magnitude of the world-class hydrothermal base metal sulfide orebody at Navan, Ireland: Economic Geology, v. 96, p. 885–890.

Holser, W.T., 1977, Catastrophic chemical events in the history of the ocean: Nature, v. 267, p. 403.

Jicha, H.L., 1951, Alpine lead-zinc ores of Europe: Economic Geology, v. 46, p. 707–730.

Koeppel, V., and Schroll, E., 1988, Pb-isotope evidence for the origin of lead in stratabound Pb-Zn deposits in Triassic carbonates of the Eastern and Southern Alps: Mineralium Deposita, v. 23, p. 96–103.

Kucha, H., 1988, Biogenic and nonbiogenic concentration of sulphur and metals in the carbonate-hosted Ballinalack Zn-Pb deposit, Ireland: Mineralogy and Petrology, v. 38, p. 171–187.

——1989, Macrotextures, microtextures, and carbonate-sulfide relationships in stratiform, carbonate-hosted Zn-Pb orebodies of Silvermines, Ireland: Mineralium Deposita, v. 24, p. 48–55.

Kucha, H., and Stumpfl, E.F., 1992, Thiosulfates as precursors of banded sphalerite and pyrite at Bleiberg, Austria: Mineralogical Magazine, v. 56, p. 165–172.

Kucha, H., and Viaene, W., 1993, Compounds with mixed and intermediate sulfur valences as precursors of banded sulfides in carbonate-hosted Zn-Pb deposits in Belgium and Poland: Mineralium Deposita, v. 28, p. 13–21.

Kucha, H., Wouters, R., and Arkens, O., 1989, Determination of sulphur and iron valence by microprobe: Scanning Microscopy International, v. 3, p. 89–97.

Kucha, H., Van der Biest, J., and Viaene, W. A., 1990, Peloids in stratabound Zn-Pb deposits and their genetic importance: Mineralium Deposita, v. 25, p. 132–139.

Kucha, H., Schroll, E., and Stumpfl, E.F., 2001, Direct evidence for bacterial sulphur reduction in Bleiberg-type deposits: Joint 6th Biennial SGA-SEG Meeting, Krakow, Poland, 2001, Proceedings, p. 149–152.

——2005, Fossil sulphate-reducing bacteria in the Bleiberg lead-zinc deposit, Austria: Mineralium Deposita, v. 40, p. 123–126.

Kuhlemann, J., Vennemann, T., Herlec, U., Zeeh, S., and Bechstaedt, T., 2001, Variations of sulfur isotopes, trace element compositions, and cathodoluminescence of Mississippi Valley-Type Pb-Zn ores from the Drau Range, Eastern Alps (Slovenia-Austria): Implications for ore deposition on a regional versus microscale: Economic Geology, v. 96, p. 1931–1941.

Labrenz, M., and Banfield, J.F., 2004, Sulfate-reducing bacteria-dominated biofilms that precipitate ZnS in a subsurface circumneutral-pH mine drainage system: Microbial Ecology, v. 47, p. 205–217.

Labrenz, M., Druschel, G.K., Thomsen-Elbert, T., Gilbert, B., Welch, S.A., Kemner, K.M., Logan, G.A., Summons, R.E., De Stasio, G., Bond, P.L., Lai, B., Kelley, S.D., and Barnfield, J.F., 2000, Formation of sphalerite (ZnS) deposits in natural biofilms of sulfate-reducing bacteria: Science, v. 290, p. 1744–1747.

Leach, D.L., Bechstaedt, T., Boni, M., and Zeeh, S., 2003, Triassic-hosted MVT Zn-Pb ores of Poland, Austria, Slovenia and Italy, *in* Kelly, J.G., Andrew, C.J., Ashton, J.H., Boland, M.B., Earls, G., Fusciardi, L., and Stanley, G., eds., Europe's major base metal deposits: Dublin, Irish Association for Economic Geology, p. 169–213.

Leach, D.L., Sangster, D.F., Kelley, K.D., Large, R.R., Garven, G., Allen, C.R., Gutzmer, J., and Walters, S., 2005, Sediment-hosted lead-zinc deposits: A global perspective: ECONOMIC GEOLOGY 100TH ANNIVERSARY VOLUME, p. 561–607.

Little, C. T. S., Herrington, R. J., Maslennikov, V. V., Morris, N. J., and Zaykov, V. V., 1997, Silurian hydrothermal vent community from the Southern Urals, Russia: Nature, v. 385, p. 146–148.

Maucher, A., and Schneider, H. J., 1967, The Alpine lead-zinc ores: ECONOMIC GEOLOGY MONOGRAPH 3, p. 71–89.

Moeller, P., 1987, Correlation of homogenization temperatures of accessory minerals from sphalerite-bearing deposits and Ga/Ge model temperatures: Chemical Geology, v. 61, p. 153–159.

Nedwell, D.B., and Banat, I.M., 1981, Hydrogen as an electron donor for sulphate-reducing bacteria in slurries of salt marsh sediment: Microbial Ecology, v. 7, p. 305–313.

Ohmoto, H., and Lasaga, A. C., 1982, Kinetics of reactions between aqueous sulfates and sulfides in hydrothermal systems: Geochimica et Cosmochimica Acta, v. 46, p. 1727–1745.

Rantitsch, G., 2001, Thermal history of Drau Range (Eastern Alps): Schweizerische Mineralogische und Petrographische Mitteilungen, v. 81, p. 181–196.

——2003, A new evaluation of fluid inclusion data based on thermal basin modeling for the Drau Range, Eastern Alps: Mitteilungen der Österreichischen Geologischen Gesellschaft, v. 93, p. 77–85.

Rees, C.E., 1973, A steady-state model for sulphur isotope fractionation in bacterial reduction processes: Geochimica et Cosmochimica Acta, v. 37, p. 1141–1162.

Rickard, D.T., 1973, Limiting conditions for synsedimentary sulfide ore formation: ECONOMIC GEOLOGY, v. 68, p. 605–617.

Robinson, B.W., and Kusakabe, M., 1975, Quantitative preparation of sulfur dioxide, for $^{34}S/^{32}S$ analysis, by combustion with cuprous oxide: Analytical Chemistry, v. 47, p. 1179–1181.

Sánchez-Román, M., Vasconcelos, C., Schmid, T., Dittrich, M., McKenzie, J. A., Zenobi, R., and Rivadeneyra, M. A., 2008, Aerobic microbial dolomite at the nanometer scale: Implications for the geologic record: Geology, v. 36, p. 879–882.

Sangster, D.F., ed., 1996, Carbonate-hosted lead-zinc deposits: Society of Economic Geologists Special Publication 4, 664 p.

Schmidt, T., Blau, J., and Kazmer, M., 1991, Large-scale strike-slip displacement of the Drauzug and the Transdanubian Mountains in early Alpine history: Evidence from Permo-Mesozoic facies belts: Tectonophysics, v. 200, p. 213–232.

Schneider, H.J., 1964, Facies differentiation and controlling factors for the depositional lead-zinc concentration on the Ladinian geosyncline of the Eastern Alps, *in* Amstutz, G. C., ed., Sedimentology and ore genesis: Developments in sedimentology: 2: Amsterdam London New York, Elsevier, p. 29–45.

Schroll, E., 1997, The Triassic carbonate-hosted Pb-Zn mineralization in the Alps (Europe): The genetic position of Bleiberg type deposits: Society of Economic Geologists Special Publication 4, p. 182–194.

——2006, Neues zur Genese der Blei-Zink-Lagerstätte Bleiberg: Carinthia II, v. 116, p. 483-500.

——2008, Blei-Zink-Lagerstätte Bleiberg. Die Geschichte ihrer Erforschung: Klagenfurt, Naturwissenschaftlicher Verein für Kärnten, 286 p.

Schroll, E., and Wedepohl, K. H., 1972, Schwefeliostopenuntersuchungen an einigen Sulfid- und Sulfatmineralen der Blei-Zink-Lagerstätte Bleiberg-Kreuth, Kärnten: Tschermaks Mineralogische und Petrographische Mitteilungen, v. 17, p. 286–290.

Schroll, E., and Pak, E., 1983, Sulfur isotope investigations of ore mineralizations of the Eastern Alps, *in* Schneider, H. J., ed., Mineral deposits of the Alps and the Alpine Epoch in Europe: Berlin Heidelberg, Springer, p. 169–175.

Schroll, E., and Rantitsch, G., 2005, Sulphur isotope patterns from the Bleiberg deposit (Eastern Alps) and their implications for genetically affiliated lead-zinc deposits: Mineralogy and Petrology, v. 84, p. 1–18.

Schroll, E., Schulz, O., and Pak, E., 1983, Sulphur isotope distribution in the Pb-Zn-deposit Bleiberg (Carinthia; Austria): Mineralium Deposita, v. 18, p. 17–25.

Schroll, E., Köppel, V., and Cerny, I., 2006, Pb and Sr isotope and geochemical data from the Pb-Zn deposit Bleiberg (Austria): Constraints on the age of mineralization: Mineralogy and Petrology, v. 86, p. 129–156.

Schulz, O., 1966, Die diskordanten Erzgänge vom "Typus Bleiberg" syndiagenetische Bildungen, Atti del Symposium Internazionale sui Giacimenti Minerari delle Alpi, Settembre, Trento, Saturnia, p. 149–162.

——1968, Die synsedimentäre Mineralparagenese im oberen Wettersteinkalk der Pb-Zn-Lagerstätte Bleiberg-Kreuth (Kärnten), Carinthia: Tschermaks Mineralogische und Petrographische Mitteilungen, v. 12, p. 230–289.

——1973, Wirtschaftlich bedeutende Zinkanreicherung in syndiagenetischer submariner Deformationsbreccie in Kreuth (Kärnten): Mineralogy and Petrology, v. 20, p. 280–295.

——1975, Resedimentbreccien und ihre möglichen Zusammenhänge mit Zn-Pb-Konzentrationen in mitteltriadischen Sedimenten der Gailtaler Alpen (Kärnten). Tschermaks Mineralogische und Petrographische Mitteilungen, v. 22, p. 130–177.

——1985, Ausgewählte Gefügebefunde in der kalkalpinen Pb-Zn-Lagerstätte Bleiberg-Kreuth (Gailtaler Alpen, Kärnten): Archiv für Lagerstättenforschung der Geologischen Bundesanstalt, v. 6, p. 91–99.

Seal, R.R., 2006, Sulfur isotope geochemistry of sulfide minerals: Reviews in Mineralogy and Geochemistry, v. 61, p. 633–677.

Siegl, W., 1957, Diskussionsbeitrag zu "Zonare Anordnung, Sonderfazies und Anlagerungsgefüge" Berg- und Hüttenmännische Monatshefte, v. 102, p. 237–238.

Southam, G., and Donald, R., 1999, A structural comparison of bacterial microfossils vs. "nanobacteria" and nanofossils: Earth Science Reviews, v. 48, p. 251–264.

Southam, G., and Saunders, J. A., 2005, The geomicrobiology of ore deposits: ECONOMIC GEOLOGY, v. 100, p. 1067–1084.

Vairavamurthy, A., Manowitz, B., Luther, G. W., and Jeon, Y., 1993, Oxidation state of sulfur in thiosulfate and implications for anaerobic energy matabolism: Geochimica et Cosmochimica Acta, v. 57, p. 1619–1623.

Wirsen, C. O., Jannasch, H. W., Molyneaux, S. J., Rona, P. A., and Thompson, G. A., 1993, Chemosynthetic microbial activity at Mid-Atlantic Ridge hydrothermal vent sites: Journal of Geophysical Research, v. 98, p. 9693–9703.

Wright, D. T., and Wacey, D., 2005, Precipitation of dolomite using sulphate-reducing bacteria from the Coorong region, South Australia: Significance and implications: Sedimentology, v. 52, p. 987–1008.

Zeeh, S., 1995, Complex replacement of saddle dolomite by fluorite within zebra dolomites: An example from Radnig, Carinthia, Austria: Mineralium Deposita, v. 30, p. 469–475.

Zeeh, S., and Bechstaedt, T., 1994, Carbonate-hosted Pb-Zn mineralization at Bleiberg-Kreuth (Austria): Compilation of data and new aspects: Special Publication of the Society for Geology Applied to Mineral Deposits, Berlin, Springer, v. 10, p. 271–296.

Zeeh, S., Bechstaedt, T., McKenzie, J., and Richter, D. K., 1995, Diagenetic evolution of the Carnian Wetterstein platforms of the Eastern Alps: Sedimentology, v. 42, p. 199–222.

Zeeh, S., Kuhlemann, J., and Bechstädt, T., 1999, The classical Pb-Zn deposits of the Eastern Alps (Austria/Slovenia) revisited: MVT deposits resulting from gravity driven fluid flow in the Alpine realm: Geologija, v. 41, p. 257–273.

Zhang, H., and Banfield, J. F., 1998, Thermodynamic analysis of phase stability of nanocrystalline titania: Journal of Materials Chemistry, v. 8, p. 2073–2076.